UNIVERSITY OF BIRMINGHAM

University of Birmingham Research at Birmingham

Kepler Mission stellar and instrument noise properties

Gilliland, Ronald L.; Chaplin, William J.; Dunham, Edward W.; Argabright, Vic S.; Borucki, William J.; Basri, Gibor; Bryson, Stephen T.; Buzasi, Derek L.; Caldwell, Douglas A.; Elsworth, Yvonne P.; Jenkins, Jon M.; Koch, David G.; Kolodziejczak, Jeffrey; Miglio, Andrea; Van Cleve, Jeffrey; Walkowicz, Lucianne M.; Welsh, William F.

[Link to publication on Research at Birmingham portal](#)

KEPLER MISSION STELLAR AND INSTRUMENT NOISE PROPERTIES

Ronald L. Gilliland[1], William J. Chaplin[2], Edward W. Dunham[3], Vic S. Argabright[4], William J. Borucki[5],
Gibor Basri[6], Stephen T. Bryson[5], Derek L. Buzasi[7], Douglas A. Caldwell[8], Yvonne P. Elsworth[2],
Jon M. Jenkins[8], David G. Koch[5], Jeffrey Kolodziejczak[9], Andrea Miglio[2], Jeffrey van Cleve[8],
Lucianne M. Walkowicz[5], and William F. Welsh[10]

[1] Space Telescope Science Institute, Baltimore, MD 21218, USA; gillil@stsci.edu
[2] School of Physics and Astronomy, University of Birmingham, UK
[3] Lowell Observatory, Flagstaff, AZ 86001, USA
[4] Ball Aerospace and Technologies Corp., Boulder, CO 80301, USA
[5] NASA Ames Research Center, Moffett Field, CA 94035, USA
[6] Astronomy Department, University of California, CA 94720, USA
[7] Eureka Scientific, Oakland, CA 94602, USA
[8] SETI Institute/NASA Ames Research Center, Moffett Field, CA 94035, USA
[9] Space Science Office, NASA Marshall Space Flight Center, Huntsville, AL 35812, USA
[10] Astronomy Department, San Diego State University, San Diego, CA 92182, USA

ABSTRACT

Kepler mission results are rapidly contributing to fundamentally new discoveries in both the exoplanet and asteroseismology fields. The data returned from *Kepler* are unique in terms of the number of stars observed, precision of photometry for time series observations, and the temporal extent of high duty cycle observations. As the first mission to provide extensive time series measurements on thousands of stars over months to years at a level hitherto possible only for the Sun, the results from *Kepler* will vastly increase our knowledge of stellar variability for quiet solar-type stars. Here, we report on the stellar noise inferred on the timescale of a few hours of most interest for detection of exoplanets via transits. By design the data from moderately bright *Kepler* stars are expected to have roughly comparable levels of noise intrinsic to the stars and arising from a combination of fundamental limitations such as Poisson statistics and any instrument noise. The noise levels attained by *Kepler* on-orbit exceed by some 50% the target levels for solar-type, quiet stars. We provide a decomposition of observed noise for an ensemble of 12th magnitude stars arising from fundamental terms (Poisson and readout noise), added noise due to the instrument and that intrinsic to the stars. The largest factor in the modestly higher than anticipated noise follows from intrinsic stellar noise. We show that using stellar parameters from galactic stellar synthesis models, and projections to stellar rotation, activity, and hence noise levels reproduce the primary intrinsic stellar noise features.

Key words: methods: observational – stars: activity – stars: late-type – stars: oscillations – stars: statistics – techniques: photometric

1. INTRODUCTION

As of early 2011 the *Kepler* mission is roughly half way through its baseline 3.5 year mission, with about one-third of the baseline data having now received some analysis. The pace of discoveries and results from the *Kepler* mission is accelerating and already quite extensive, even though the prime goal of detecting true Earth-analog exoplanets remains in the future, simply from needing to have more extensive time coverage in order to detect transits spaced by a full year. In the area of exoplanets, over 1200 candidates have been detected and reported in Borucki et al. (2011), with validation of exoplanets first following from transit timing variations discussed by Holman et al. (2010), the smallest rocky planet to date in Batalha et al. (2011), and a six-planet system unveiled in Lissauer et al. (2011). Discoveries from *Kepler*'s second area of emphasis are equally impressive ranging from detection of oscillations on solar-type stars for hundreds of cases in Chaplin et al. (2011a) (only tens had been known before the *Kepler* mission) to detailed inferences on individual stars (Metcalfe et al. 2010; Kurtz et al. 2011), and a recent breakthrough involving the detection of both the expected *p*-modes as well as *g*-modes allowing sensitive new studies of red giant stars (Bedding et al. 2011; Beck et al. 2011). In stellar astrophysics, *Kepler* has revealed a remarkable eccentric A-star binary viewed nearly face on with reflected light

features superimposed on tidally forced *g*-mode oscillations (Welsh et al. 2011), and two instances of mutually eclipsing hierarchical triple systems (Carter et al. 2011; Derekas et al. 2011).

Returning to a discussion of the prime goal of detecting true Earth-analogs, the observational quest is truly daunting. An Earth-analog presents a transit signature with a depth of 85 parts per million (ppm), lasting a statistical average of 10 hr, and occurring once per year. The signal would only be evident after seeing three successive transits equally spaced in time. Since the geometric probability of having transits in Earth-analog systems is only 0.5%, it is necessary to monitor a very large number of stars nearly continuously over multiple years at very high precision to have any chance of success. The *Kepler* mission was scoped (Koch et al. 2010) to be able to determine the frequency of Earth-size planets at sufficiently long orbital periods to reach well into the habitable zone (Kasting et al. 1993). This is challenging on a number of levels, including perhaps the simplest one of the noise levels needed to support detection. Notable in the Borucki et al. (2011) paper is a significant fall-off in planet frequency for the smallest planet candidates, especially at the long orbital periods associated with habitability (possible presence of liquid water on the surface based on equilibrium temperatures). Some of this fall-off is expected to date, since insufficient time has passed to be able to

detect true Earth analogs. However, the relative sparsity of Earth-sized planets at shorter orbital periods is open to interpretation and will surely be the focus of much discussion in the exoplanet community. Do the statistical trends primarily follow from the physics of planet formation (Gould & Eastman 2011; Ida & Lin 2004), or is there a strong contribution from observational incompleteness given the larger than anticipated noise levels (Jenkins et al. 2010b; Christiansen & Machalek 2010)? This question is beyond the scope of this paper to resolve. We will endeavor to more fully explore the noise levels obtained in the *Kepler* mission given that these are not as low as expected.

The approach in the remainder of the paper is as follows. A self-contained introduction to the mission and data characteristics will be given in Section 2. Based on consideration of the *Kepler* data set itself, and knowledge of instrument characteristics such as detector readout noise, a subset of ∼12th magnitude stars will be used to establish a decomposition of noise into temporal, instrument, and intrinsic stellar terms in Section 3. Section 4 will provide simulations of intrinsic stellar noise as a means of assessing the reasonableness of the noise separation, and for motivating what may be learned about stellar astrophysics from the *Kepler* results. A fainter sample of stars will be reported on in Section 5. Prospects for confirmation of the stellar noise differences found will be touched upon in Section 6 with a summary in Section 7.

2. *KEPLER* OBSERVATIONS AND NOISE METRIC

Characteristics of the *Kepler* mission have been presented in detail in Koch et al. (2010) with details on the pipeline processing given in Jenkins et al. (2010a). The overall instrument performance is discussed by Caldwell et al. (2011), with target selection covered by Batalha et al. (2010), operations by Haas et al. (2010) and initial data characteristics given by Jenkins et al. (2010b) and Gilliland et al. (2010). Ciardi et al. (2011) provide a general survey of stellar variability based on the first full month of *Kepler* data. Here we discuss some of the characteristics that are most pertinent to understanding the overall noise levels, both those arising from fundamental limitations like Poisson statistics on the sources, and simple instrument limitations such as CCD readout noise. We consider only the long cadence (LC) data, which consist of summations of 270 individual readouts each a little over 6 s long into 29.4 minute intervals. In addition, we limit our attention to those intermediate time scales that are most relevant for the detection of transits. At the high-precision levels provided by *Kepler* it has been found that all red giants are obvious photometric variables (Koch et al. 2010); we will endeavor to ignore these and other classes of variable stars by restricting our attention to roughly solar-type stars.

The *Kepler* field of view was carefully selected to fall relatively near, but not on, the galactic plane. This provides a high stellar density of dwarf stars, while avoiding too high a density of fainter background stars, which could lead to false positives through diluted eclipses of background binaries. The primary range of stellar brightness followed by *Kepler* is $Kp = 9$–15 (Koch et al. 2010), where Kp represents a broad bandpass from about 420 to 900 nm roughly a combination of V plus R bandpasses. Saturation occurs at about $Kp = 11.5$, but conservation of charge is preserved beyond saturation and excellent photometry is easily recovered from targets up to 7 mag beyond saturation by summing over the pixels bled into—along columns (Gilliland et al. 2010). For special applications on highly variable stars, observations to at least

20th magnitude may be useful. The point design for *Kepler* is based on results at 12th magnitude, and we will concentrate on stars with $Kp = 11.5$–12.5 for which fundamental noise terms, instrument contributions, and intrinsic stellar noise may be comparable in scale, thus facilitating unique determination of the separate levels.

The primary noise metric for *Kepler* is referred to as CDPP, combined differential photometric precision, which is intended to be either the observed noise in a carefully specified temporal domain, or the predicted noise level in the same temporal domain from rolling up all contributing factors including intrinsic stellar variability—see Jenkins et al. (2010b) for discussion of early on-orbit results. By design CDPP near 6.5 hr (one-half the time for a central transit of a true Earth-analog) was intended to be about 20 ppm for the mode of dwarf stars at 12th magnitude, in order to provide slightly more than 4σ signal-to-noise ratio for single transits with 85 ppm depth. With four such transits the overall detection statistic (Jenkins 2002) would then reach a level providing less than one statistical false positive over the whole ensemble of such stars searched for transits. In reality (Christiansen & Machalek 2010), the CDPP assessed as the mode over 12th magnitude dwarf stars is about 30 ppm, or 50% higher than planned for. Based upon considerations of solar variability in the relevant temporal domain (Jenkins 2002), stars were allocated 10 ppm in the noise budget to be rolled up into the CDPP. With a Poisson term due to counting some $4.5 \times 10^9 \, e^-$ per 6.5 hr at 12th magnitude equal to about 15 ppm, the stellar noise was expected to be a significant contributor to the total noise, but not usually a limiting factor. A tail to higher intrinsic stellar noise was anticipated from more active, typically younger stars.

Having determined the observed CDPP for a star, or ensemble of such stars, how would one determine what part of this is intrinsic to the star? Answering this question will take up most of Section 3. We continue here with an introduction to the observations and data characteristics that will need to be accounted for and analyzed fully to address this.

The *Kepler* data are collected in segments one-quarter of the 372 day spacecraft-year long. *Kepler* is in an Earth-trailing orbit which provides unobscured access to a field well off the ecliptic throughout the year. In order to keep the solar arrays illuminated, successive $90°$ rolls are executed every one-quarter year. The focal plane consists of 42 CCDs with $27 \, \mu$ pixels (with very deep wells of about $1.1 \times 10^6 \, e^-$) and 1024×2200 rows and columns. Each CCD has two readout amplifiers leading to a total of 84 channels. The CCDs are mounted pairwise into 21 modules which cover a 5×5 grid except for the corners which have smaller pixel scale CCDs used only for precisely guiding the spacecraft. The CCDs are oriented such that rotational symmetry is maintained except for the central-most module. Although stars fall on a unique detector during each observing quarter, they maintain the same symmetry with respect to rows, columns and stellar neighbors after each roll (except for the central module where the stars always remain, and symmetry is broken).

Figure 1 is used for several orientation purposes to the *Kepler* observing procedure and basic characteristics of the instrument. The layout of CCDs illustrates the rotational symmetry across observing quarters. Of greater relevance for this paper is to note the four channels in Figure 1 flagged as comprising one "quartet." For this example a star on channel 1 in Quarter 2 (2009 July–September) would be moved to channel 53 for Quarter 3 (2009 October–December), then channel 81 for Quarter 4
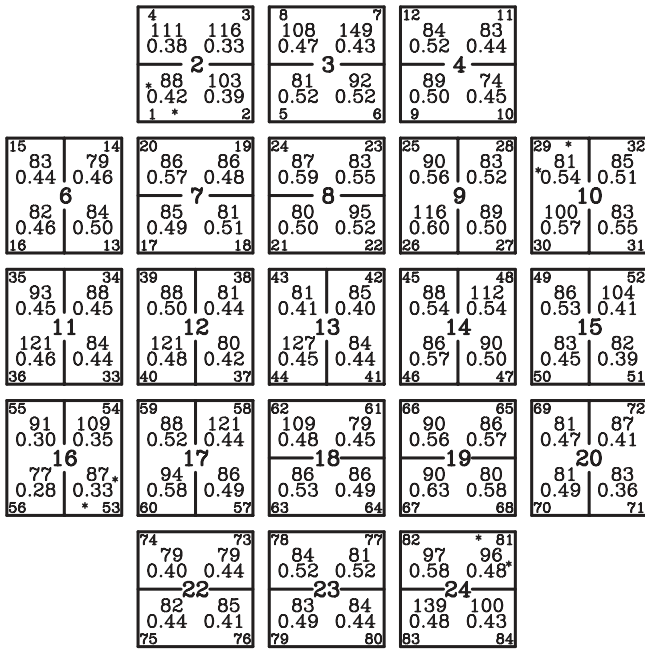
Figure 1. Schematic layout of the 42 CCDs comprising the science array for *Kepler*. The CCDs are mounted pairwise into 21 modules labeled consecutively 1 through 25 except for the missing corners which have non-science CCDs used only for guiding. Within a module each CCD is read out by two amplifiers which are shown on the same side of a dividing line. The CCDs are laid out to maintain symmetry of rows and columns as the spacecraft is rotated by 90° (except for central module lacking this symmetry). Numbers in the corners of each module are channel numbers 1 through 84. The pairs of numbers near the center of each channel are (top) readout noise in electrons, and (bottom) PSF energy content of central pixel for a centered star. Note that channels 1, 29, 81, and 53 are flagged with a pair of "*," these comprise a logical quartet as discussed in the text.

(2010 January–March), then channel 29 for Quarter 5 (2010 April–June), before starting the cycle over on channel 1 for Quarter 6 (2010 July–September). The stars that started in Quarter 2 on any one of channels 1, 29, 53, and 81 will simply permute through these same channels and thus form a natural "quartet." There are 21 such quartets, and analysis of the stars within quartets will play a key role in the noise decomposition discussed in the next section.

Also presented in Figure 1 are numerical values by channel for readout noise in electrons for each amplifier and a metric of the focus as the fraction of energy contained in the central pixel for a star centered on a pixel. Readout noise levels range from 77 to 149 e^- and are taken from van Cleve & Caldwell (2009). The central pixel energy fractions were derived by the first author from images taken during commissioning, after the primary mirror had been adjusted in tilt and piston to attain best focus. A check with Q5 data one year later showed nearly identical focus values.

The 27 μ CCD pixels span a scale of 3″.98 on the sky, very large compared to the diffraction limit of the 0.95 m Schmidt telescope. Initial plans had called for the telescope point-spread function (PSF) to be soft, specifying a maximum flux of some 30% in the central pixel of a best focused star centered on a pixel. Mid-way through mission development this was reconsidered. Sharper PSFs would help both in terms of avoiding large numbers of false positives through background eclipsing binaries and optimally supporting through-transit centroiding to eliminate most background eclipsing binaries as false positives that blend with the targets. The resulting *Kepler* PSFs are very sharp—several of the modules have central

energy concentrations for a central pixel in excess of 50%, with the sharpest focus channels reaching above 60%. The channels with the worst focus still come in near 30% central pixel energy fraction, with a mean over the full array being at 47%. By contrast *Hubble Space Telescope* (*HST*) imaging instruments such as Advanced Camera for Surveys (ACS) or WFC3 have typical central energy fractions more like 20%—for a mission intended to have high resolution as a primary attribute. Simulations and now experience have both indicated that the best photometry is obtained from the *Kepler* channels having the better focus. While the *Kepler* PSFs are severely undersampled (in many cases with the underlying FWHM of the optical PSF being only one-quarter of a pixel), the spacecraft guiding at the pixel scale is exquisite, much better than the already impressive case of *HST*. On the timescales most relevant for transits and CDPP the spacecraft jitter is about 6×10^{-5} pixels. The point-to-point jitter of the *Kepler* observations is $\sim 1.2 \times 10^{-4}$ pixels. For *HST*, point-to-point jitter on comparable timescales is ~ 0.1 pixels (Gilliland 2005) on the much finer 0″.05 pixel scale of ACS. In an absolute sense the *Kepler* jitter bests *HST* by a full order of magnitude. Translated to pixel scale, the *Kepler* advantage is three orders of magnitude. On longer timescales of months differential velocity aberration can move images by over half a pixel in extreme cases over one quarter. The *Kepler* PSFs average about 4 pixels in diameter for 95% encircled energy, thus allowing apertures used for photometric extractions to remain small.

At 12th magnitude the average stellar image will consist of 12–13 pixels forming the "optimal aperture." A "postage stamp" of pixels including this optimal aperture used for the photometric extraction plus a buffer halo of 1–2 pixels radius is returned for each target. This optimal aperture is held fixed within each quarter and is selected to maximize the signal-to-noise of each star for simple aperture sum photometry which is the only method used in the pipeline (Bryson et al. 2010a). The *Kepler* CCDs have large readout noise levels by ordinary standards, at about 100 e^-. Furthermore, each LC observation consists of 270 individual integrations. Therefore, the total variance from readout noise on a 12th magnitude star in the 6.5 hr intervals for which CDPP is defined sums to about 4.5×10^8 electrons squared, but this is only one-tenth the variance (direct counts) from Poisson statistics on the target itself. The number of pixels used for the optimal aperture of a star each quarter is a complex function of the PSF, and whether a target has nearby neighbors, see Bryson et al. (2010b).

At the middle of the 3.5 year baseline mission the overall spacecraft status is healthy. The only significant degradation to date was the loss of the two CCDs on module 3 about nine months into the mission, about one month into Quarter 4. The associated electronics failure is not expected to affect other modules.

We adopt a noise metric that is very similar to the formal, wavelet-based CDPP evaluated in the *Kepler* Science Operations Center pipeline (Jenkins et al. 2010b), but easier to compute and explain. Our noise metric starts with the pipeline calibrated, or PDC (Presearch Data Conditioned) light curves archived for the project at the Multimission Archive (MAST) at STScI.[11] These data are then subjected to a high-pass Savitsky–Golay filtering by fitting a quadratic polynomial 2 days (97 LC points) wide centered on each point in the time series, then subtracting this. Sigma-clipping is introduced at 5σ to eliminate highly

___
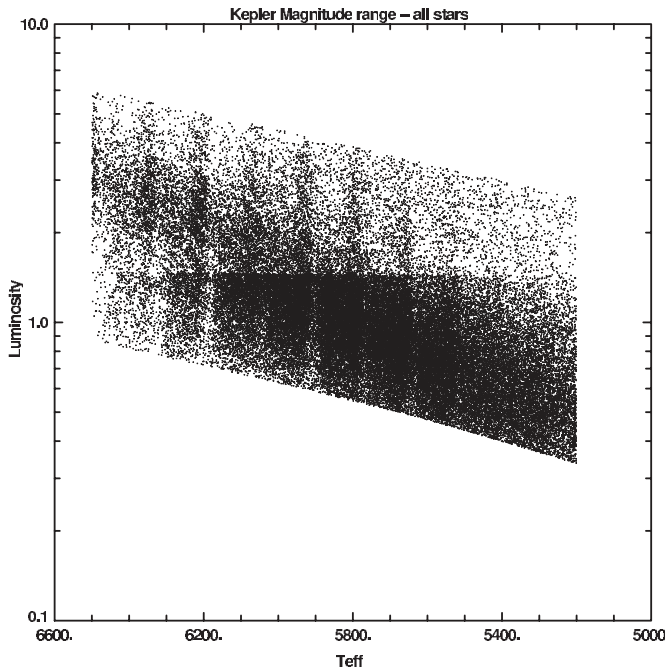
[11] http://stdatu.stsci.edu/kepler/

Figure 2. HR diagram for the 69,005 stars retained for this study after eliminating sub-giants, giants, eclipsing binaries, KOIs, etc. as discussed in the text. Luminosity is in solar units.

Figure 3. Distribution of the 69,005 retained stars in galactic coordinates.

deviant points. Then the data are block-averaged into 6.5 hr segments by forming successive averages over 13 consecutive LC intervals. Only segments containing at least seven valid intervals are retained. The CDPP is simply obtained as the standard deviation of the 6.5 hr means. The Savitsky–Golay filter suppresses (based on direct tests with trial time series) 16.8% of the expected rms from white Gaussian noise for 6.5 hr bins, this is corrected for by multiplying the resulting CDPP by ×1.168 to adjust for how much white noise would be suppressed by this bandpass filtering. We thus end up with a strongly bandpass-limited metric, having first removed any slow variations captured by a 2 day wide least-squares quadratic fit, then averaging out all time scales shorter than 6.5 hr. The scale of this CDPP is nearly identical to the 12 hr CDPP provided by the SOC pipeline, and about 15% smaller than the 6 hr CDPP from SOC. Agreement between the two estimates is quite good with a 1σ scatter of 10%.

Such a CDPP measure is formed for each star of interest separately for each of Quarters 2 through 6. Q1 was omitted because it was less than half a quarter, and Q0 was an even shorter commissioning period using a non-standard target set. Module 3 was lost about three weeks into the start of Q4; these truncated time series are also omitted.

For our purposes of determining what components of noise should be ascribed to the stars themselves, or other factors, we restrict attention to stars that are not known a priori to be variable. At the precisions reached by *Kepler* all red giants are variable (Koch et al. 2010; Gilliland 2008). Many stars hotter than 6500 K fall into the classical instability strip and will be variable. Some stars are known to have variability in their light curves from being eclipsing binaries, or *Kepler* objects of interest hosting planet candidates. We start with the roughly 165,000 full list of *Kepler* stars and adopt the *Kepler* Input Catalog (KIC; Brown et al. 2011) parameters. The approximately 15% of stars in the KIC that are not "classified," i.e., do not have $T_{\rm eff}$, gravities, etc.,
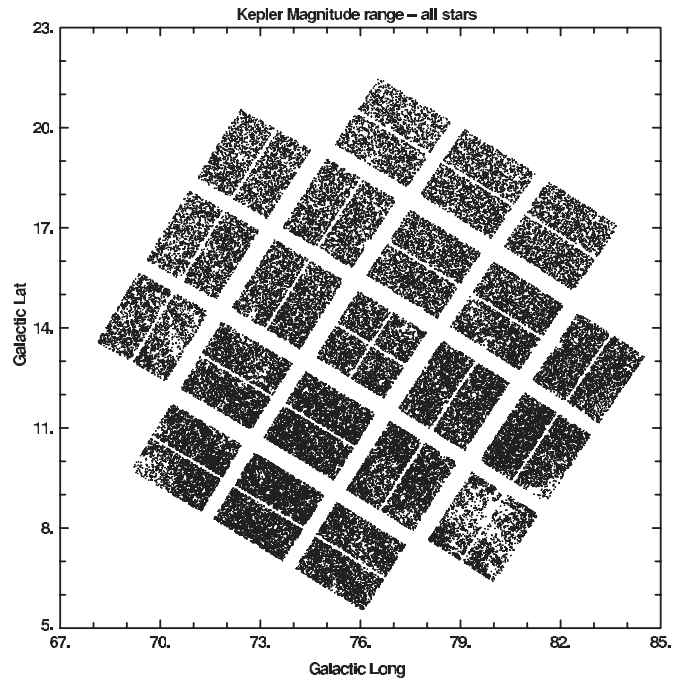
are dropped from consideration. We evaluate the predicted $\nu_{\rm max}$ value (location in a power spectrum of largest p-mode amplitudes which in the Sun is at 3150 μHz) of solar-type stellar oscillations and keep only the set between 1000 and 6000 μHz, thus quite effectively eliminating both giants and subgiants from the sample (see Chaplin et al. 2011b). $\nu_{\rm max}$ is proportional to gravity modified by $T_{\rm eff}^{-1/2}$; our sample has been chosen to have $\log g \sim 4.0$–4.7. We also require that the $T_{\rm eff}$ be between 5200 and 6500 K, and that mass be less than 1.4 $M_\odot$. The resulting list is then cross-correlated with the known EBs and KOIs and all of these are dropped. Stars are further restricted to have a maximum contamination over the multiple quarters of less than 20%, i.e., at least 80% of the light in optimal apertures is thought to come from the target star rather than light from nearby neighbors. With all of these eliminations in place a list of 69,005 stars remains.

At $Kp = 11.5$–12.5 used for primary results in this paper, very few stars have large contamination levels. Only 1% of 12th magnitude stars are above the 20% cut, and only 1% of the retained sample exceed a 10% contamination.

Figure 2 shows the distribution of retained stars in an HR diagram. Luminosity follows from the KIC mass, $\log g$, and $T_{\rm eff}$. The upper boundary follows from $\nu_{\rm max} = 1000 \mu$Hz, while the lower boundary is set by the complementary $\nu_{\rm max}$ limit. The distribution in galactic coordinates is shown in Figure 3, and the CDPP averaged over Quarters 2 through 6 is shown for this set of 69,005 dwarf stars in Figure 4. The noise distribution in the lower panel of Figure 1 from Jenkins et al. (2010b) may be compared directly with Figure 4. A primary feature of the Jenkins et al. (2010b) figure (a horizontal swath of stars variable at a few hundred ppm) is not included in our Figure 4 as a result of excluding giants and subgiants.

The CDPP, formed for each star as the mean over Quarters 2–6 after excluding the maximum value, is shown in Figure 5 as distributions over galactic latitude and the fractional distribution with noise level. CDPP shows a broad distribution with a mode of 25 ppm, with overall median (from set to CDPP < 100 ppm)
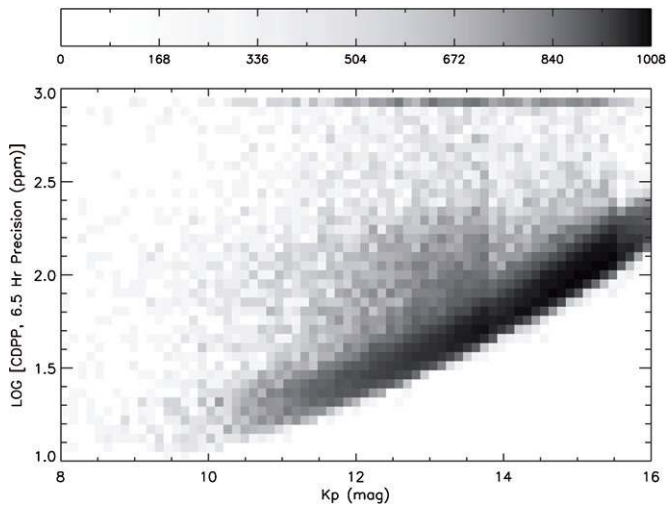
Figure 4. Scatter of CDPP proxies as discussed in the text for the 69,005 retained stars, all of which are believed to be dwarfs of roughly solar-type based on KIC parameters. Known binaries and KOIs were not included. The noise values are averaged over Quarters 2 through 6. The band at top includes all cases at and above this level. The bar at top defines the density of stars per 0.1 (mag) × 0.05 (log CDPP) bin.

Figure 5. Upper panel shows the CDPP in ppm for the $Kp = 11.5$–12.5 sample as a function of galactic latitude. Medians evaluated over up to 100 ppm are shown as "o," while means from up to 3× the median at each degree of galactic latitude are shown as "+" symbols. Standard errors for the means are shown. The lower panel shows a histogram of fraction of stars per ppm bin.

of 27.9 ppm. The overall mean evaluated over a range to 3× the median is 32.0 ± 0.3 (s.e.) ppm.

3. STELLAR AND INSTRUMENTAL NOISE DECOMPOSITION

The $Kp = 11.5$–12.5 mag range will be used for primary analyses here. Our goal is to achieve separation of the several terms most important for determining the observed noise (CDPP) level of stars. Within the 12th magnitude band we have about 2500 dwarf stars in our sample, most of which were observed five times (a small subset was lost in Quarter 4 and after from the loss of module 3, and a minor geometric distortion of the focal plane leads to stars falling on or off silicon at the <1% level quarter-to-quarter), there are thus some 12,500 observables. We wish to solve for five parameters corresponding to any unique extra noise quarter-to-quarter, 84 parameters corresponding to extra noise that may be associated with individual channels, and the 2500 intrinsic stellar noise values. Such a decomposition can be easily set up as a general least-squares problem with the normal equations having some 2589 unknowns and 12,500 observables. While formally overdetermined, the problem possesses multiple degeneracies. This forces us to use some finesse in obtaining a decomposition.

We work primarily in variance space where we assume that the different noise terms are uncorrelated and can therefore simply be added. For quoting results we will often use noise estimated as the square root of variance.

The first step in all decompositions is to express the observables as variances, simply by squaring the CDPPs available in ppm. The next step is to remove deterministically set terms for Poisson noise from the target and sky, and detector readout noise. This combined noise term for the target is set as the inverse of the projected signal-to-noise ratio. The signal term uses the median value in e^- for the PDC (in archival time series these are the "ap_corr_flux" vectors) light curve (which has had an offset ascribed to neighbors removed in the pipeline). In the sum of variances for noise the median value of the "raw" light curve ("ap_raw_flux" vector) is used since the excess flux in the optimal aperture due to neighboring stars will at the least contribute extra Poisson noise. As an equation the combination of Poisson noise from target and sky, plus detector readout noise, is:

$$\text{Noise (ppm)} = 10^6 (\text{raw}_{\text{cts}} + \text{readout} + \text{sky})^{1/2} / \text{PDC}_{\text{cts}}, \quad (1)$$

where all terms are sums over appropriate numbers of exposures and pixels. The term for detector readout variance is the product of number of reads in 6.5 hr ($13 \times 270 = 3510$) multiplied by the number of pixels in the optimal aperture for the star in a given quarter, and then multiplied by the square of the readout noise as shown in Figure 1. The resulting readout variance is about a factor of 10 smaller than the Poisson variance for a 12th magnitude star. The contribution from Poisson noise on the accumulated sky background is another factor of several smaller. The variances passed forward for further analysis are now the observed variances (i.e., CDPP squared) from which the Poisson and readout noise have been subtracted.

3.1. Quarter-to-quarter Variations

Each quarter (~90 days) of *Kepler* observations will be unique. Some quarters, such as number 2, suffered from a larger number of spacecraft safing events than usual, and during this quarter variable guide stars were still leading to minor variations of the guiding having print-through effects on the photometry for some stars. Finally, until mid-way through Quarter 3 a spacecraft heater was operated in a way that introduced minor guiding errors on a timescale influencing CDPP; this was compounded by larger than average focus changes occurring during Q3. These and other issues with the data are detailed in the "Data Release Notes," e.g., Christiansen & Machalek (2010) for Quarter 2 that may be found at the MAST *Kepler* Archive.

Seeking quarter-to-quarter mean offsets we start by evaluating our sample of about 2500 12th magnitude stars to determine what their mean variance was in each quarter. We have also

Table 1
Quarter-to-quarter Excess Variance

Quarter	Q2	Q3	Q4	Q5	Q6
Variance	210.46	105.82	44.52	0.00	29.89
Noise	14.51	10.29	6.67	0.00	5.47

Note. Variances in ppm^2 and noise levels in ppm over the five quarters of *Kepler* data analyzed.

set up the full set of normal equations and directly solved for the quarter-to-quarter variance offsets using singular value decomposition codes (Press et al. 1992). The two approaches gave nearly identical results. Table 1 records the by-quarter variance excesses, and equivalent excess noise relative to the quietest quarter (Q5), which has been set to zero. The resulting variations are consistent with expectations given improved management of the spacecraft from Q2 to Q3 and beyond.

3.2. Channel-to-channel Instrument Noise

We have already accounted for ordinary CCD readout noise and always subtract this term as deterministic before searching for more subtle contributions. While the *Kepler* CCDs are excellent for their intended purpose, a few of them suffer from excess noise due to a number of limitations with the electronics. The Data Release Notes discuss these (Christiansen & Machalek 2010). For our purposes we simply wish to solve for the excess noise that may exist channel-to-channel without making reference to the detailed reasons for such.

Our solutions are developed on a quartet-by-quartet basis, e.g., the set of channels 1, 29, 53, and 81 which comprise one of 21 quartets. Over the five quarters the same sets of stars are seen by each of these channels in turn. A degeneracy exists between the global offsets between all four such channels and a global offset for the approximately 120 stars per quartet

observed each quarter at 12th magnitude. We can solve for these channel-to-channel offsets and do so using first SVD, followed by a direct solution of the normal equations for which the least noisy channel has been fixed to zero excess noise to remove the degeneracy. Doing this over all 21 quartets then results in *relative* offsets for the channels within the quartets, and we additionally track the median value (within the range of 0–70 ppm) of the stars for each quartet.

Table 2 provides first a mapping of channels contained in each of the 21 quartets, then the channel-to-channel offsets found from the above prescription as well as the resulting median for the stars in this quartet. We will return to further discussion of this nature, but note that channels showing unusually high-excess variance correlate at least qualitatively with channels already suspected of poorer than average performance. For example, channel number 58 (in third channel of quartet 14) is known from ground testing to have the worst overall performance in terms of image artifacts arising from limitations in the electronics boards, and the excess variance for this channel is clearly on the high side of values in Table 2. In a similar way, the channels with the poorest overall focus, starting with the worst are 56, 55, 3, 53, 54, and 4 with variances of 250, 227, 247, 192, 210, and 216 ppm^2, respectively, thus corresponding to several of the overall largest terms.

3.3. Intrinsic Solar Noise

We develop intrinsic noise levels for the Sun using 12 yr of measurements with the VIRGO/SPM instrument in the green wavelength channel onboard the ESA/NASA *SOHO* spacecraft (Fröhlich et al. 1997). We divided the 1996–2008 SPM light curve, which spans a full solar cycle, into 30 uninterrupted bins 91.7 days long with intrinsic cadence of 60 s, then binned these into 29.4 minute sums (by averaging 30 consecutive points with weights of 0.7 for the end points). These sets of data were then treated in an identical manner using the same codes to arrive

Table 2
Channel-to-channel Variance and Stellar Ensemble Offsets

Quartet	Ch1	Ch2	Ch3	Ch4	Var1	Var2	Var3	Var4	Stellar	N_{star}
1	1	29	53	81	140.90	54.99	192.28	0.00	402.58	110
2	2	30	54	82	98.56	142.10	210.43	0.00	239.58	110
3	3	31	55	83	247.34	54.76	227.10	0.00	388.34	109
4	4	32	56	84	216.59	209.20	250.18	0.00	371.60	106
5	5	33	49	77	0.00	89.25	67.81	34.47	255.40	137
6	6	34	50	78	30.65	30.40	11.43	0.00	375.71	120
7	7	35	51	79	222.62	27.85	0.00	122.56	415.36	99
8	8	36	52	80	99.47	175.74	107.77	0.00	459.71	116
9	9	13	69	73	0.00	48.47	8.15	48.41	341.25	121
10	10	14	70	74	107.84	21.19	0.00	69.57	446.70	114
11	11	15	71	75	158.94	42.07	0.00	131.08	497.34	109
12	12	16	72	76	32.50	96.09	38.06	0.00	485.31	109
13	17	25	57	65	12.23	28.59	29.61	0.00	286.63	134
14	18	26	58	66	21.57	74.67	194.93	0.00	318.53	114
15	19	27	59	67	53.40	36.42	3.79	0.00	337.93	135
16	20	28	60	68	0.00	59.28	56.96	39.63	346.57	113
17	21	37	45	61	12.29	69.33	0.00	51.35	403.00	110
18	22	38	46	62	39.93	65.51	0.00	154.15	399.32	117
19	23	39	47	63	0.00	65.34	10.18	28.90	402.67	133
20	24	40	48	64	0.00	106.90	43.89	76.42	334.28	124
21	41	42	43	44	0.00	35.26	61.98	102.74	435.70	100

Notes. After a leading column with serial number, the next four columns establish channel numbers included, which the next four columns provide by-channel variance excesses. The final two columns are median variance of the stellar ensemble for the quartet and the number of stars.
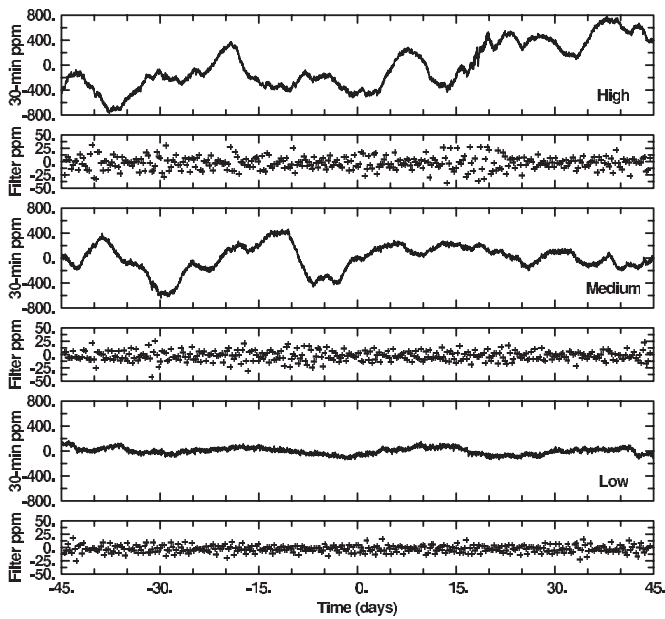
Figure 6. Solar data from VIRGO/SPM (Fröhlich et al. 1997) are shown for three 90 day blocks as variations in ppm around a median. The upper panel in each shows the direct data after binning to *Kepler*'s 29.4 minute cadence and scaling by ×0.8 as a color correction as discussed in the text. The companion panels show the data after applying the Savitsky–Golay filter followed by 6.5 hr binning used to form CDPP. The upper panel pair shows the noisiest 90 day period centered on 2002.39 (CDPP = 14.7 ppm), the middle panel pair is centered on 2005.52 (CDPP = 10.9 ppm), while the low noise case (CDPP = 7.8 ppm) is from 2007.77.

Figure 7. Each panel shows the fractional distribution of $Kp = 11.5$–12.5 stars within 1 ppm bins for intrinsic stellar noise. The mean and rms distribution for solar noise levels over quarter-long intervals spanning a solar Cycle are shown by the "+" and heavy horizontal line, with the full extent of solar noise per quarter the thin line. From top the quartet stellar variance medians are set to the minimal value (see the text) of 300 ppm^2, the 340 ppm^2 value we adopt as most representative, and the bracketing 378 ppm^2 on the high side at the bottom.

at CDPP estimates. In the case of these SOHO data instrument contributions to the variance are negligible and these estimates provide a good measure of the intrinsic variability of the Sun on the timescales of interest for this study.

The VIRGO/SPM green channel is at a wavelength of 500 nm, 5 nm wide. We thus need to correct for the differing wavelengths of the SOHO and *Kepler* observations assuming the canonical linear scaling of amplitude with wavelength (Kjeldsen & Bedding 1995). The *Kepler* bandpass is very broad covering 423–897 nm at the 5% points (Koch et al. 2010). Integrated over the spectral energy distribution for a solar-type star the mean wavelength for *Kepler* observations is 634 nm (van Cleve & Caldwell 2009). We therefore scale the derived CDPP values from the VIRGO observations down by 500/634 to approximate the variability for the *Kepler* bandpass. This provides a mean and rms of 11.0 ± 1.5 ppm, with the full range of variations encountered over the solar cycle spanning 7.8–14.7 ppm—see Figure 6. These values will be used for comparison with the distribution of stellar noise as observed for ensembles of stars with *Kepler*.

3.4. Imposing Normalization Over Channel Quartets

The variance normalizations appearing in Table 2 assume that the quietest channel of each quartet has no excess variance. Most such channels will in reality have non-zero and positive excess variance. Currently there is a direct degeneracy within each quartet between the value for the channel forced to zero and the overall level of stellar variance (as given by the median over 0–70 ppm) for all stars within the quartet.

The ~120 stars within each quartet are usually drawn from widely different and symmetric positions on the sky. Therefore, even if there were intrinsic large-scale (but low order, say a gradient over the field) variations of the stellar noise spatially,
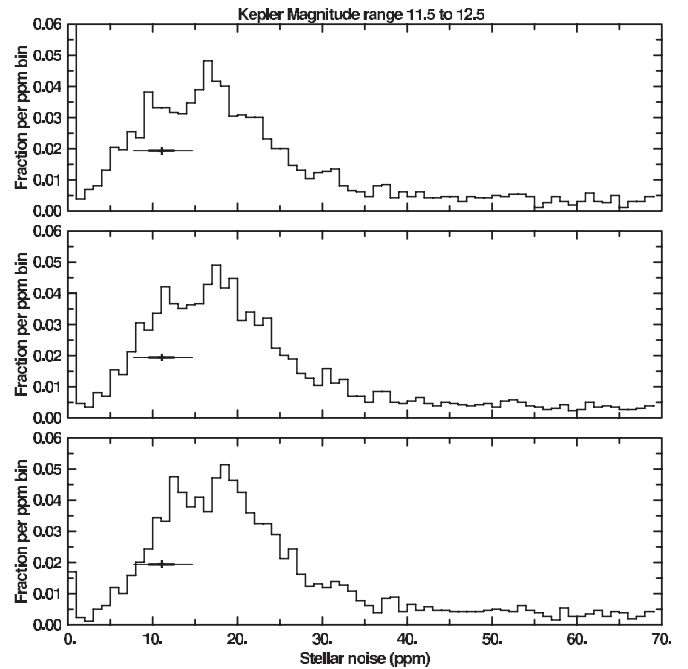
we should expect the quartets to all have similar levels of stellar variability. This provides a good and physically reasonable, albeit imperfect, means of renormalizing the variance levels within each quartet: we force the stellar medians to have a common value for all quartets via simple addition. This brings the full distribution of channel-by-channel variances to a common scale. The stellar variances are also brought to a common scale, although simple gradients of intrinsic variation across the focal plane should be preserved by this step.

The problem at hand thus becomes one of determining what single number to adopt for the stellar quartet medians. The overall minimum of the 21 by-quartet stellar variance medians is 240 ppm^2, at quartet no. 2, and may be thought of as the minimum value for this parameter, although this choice would lead to a large fraction of stars with apparent negative intrinsic variance. If instead we chose this value to be the overall mean of 378 ppm^2 for the stellar medians over all 21 quartets, then quartets 2, 5, and 13 with low values of the stellar median would develop many channels with negative variance for the instrument noise contribution.

There does not seem to be a well-defined quantitative approach to selecting this normalization. We will rather rely on showing the sensitivity to this choice and bringing in congruence with solar variability to support our ultimate selection.

Figure 7 shows the fractional distribution of noise values with three different choices of the normalization for the stellar median, from a minimal value of 300 ppm^2 at top to 378 ppm^2 at the bottom. Such changes in the overall variance zero point between possible instrument terms and noise intrinsic to the stars makes a noticeable difference for the really quiet stars, but has much less influence on stars with higher intrinsic variability.

The distribution of stellar noise seems to be bi-modal in character, with one peak in the neighborhood of typical solar

variations, and a second peak at some 5 ppm higher values. In addition, an extended tail to higher intrinsic noise exists for the more active stars.

We adopt the 340 ppm^2 variance level for the median intrinsic stellar noise over 0–70 ppm. Having done this we may now present the results of Table 2 in a different way. Values in the column "Stellar" would now all be 340 by design. Fifteen of the 21 quartets have stellar median values above 340, for these the by-channel variances will be shifted to more positive values as the difference between these entries and 340. There are six quartets for which the stellar median is smaller than this target of 340 ppm^2 which has the consequence that at least the channels starting with zero variance will shift to non-physical, negative variance values.

To assess how concerned we should be by finding a few channels coming in at negative additional variance it is useful to determine the noise levels that apply to the by-channel variance numbers in Table 2. We have done this by opening the magnitude range up slightly from 11.5–12.5 to 11.2–12.8 Kp, thus doubling the number of available stars. Then we have repeated the analyses leading to Table 2 independently for stars with even or then odd KIC numbers. As expected this led to two sets each about as large as the number of stars in the Table 2 sample. The gross features of derived values in these even and odd sets are very similar; channels standing out as high in Table 2 are high in each of the even and odd test sets, as they are for the distribution of stellar medians by quartet.

The overall rms across the variances between the even and odd sets, after shifting all for consistency with a common stellar median of 340 ppm^2, is 60 ppm^2. The estimated standard deviation on the direct values in Table 2 would be a factor of two smaller than this, or 30 ppm^2 as a general confidence level estimate. Following correction to a common stellar median of 340 ppm^2 in Table 2 entries a total of 12 channels have formally negative variances, and 5 of these are more negative than the nominal 1σ level.

The number of channels coming in with negative variance does not seem inconsistent with expected fluctuations given our measurement precision channel-to-channel. Similarly, in Figure 7 at the nominal 340 ppm^2 median value some 4% of the stars overall have entries in the first bin which corresponds to those with a negative variance. Stars with negative variance may arise from any channels that have significant gradients of intrinsic noise. Then a quiet star, on the less noisy part of the channel could be driven to negative variance when the correction for the channel as a whole is applied. Also, in some cases PDC will overfit and remove actual noise, but this is not thought widespread.

The existence of a small fraction of channels ascribed a negative intrinsic variance, and a few stars determined to have intrinsic variances less than zero, both of which are non-physical, is a signal that our determinations of these quantities introduce some broadening of intrinsic distributions.

3.5. Dependence of Stellar Noise on Galactic Latitude

The overall results for intrinsic stellar noise for the 12th magnitude sample may be seen in Figure 8. The noise has a moderate dependence on galactic latitude, and apparently bi-modal peaks near 11 and 17 ppm, with a tail to larger values. From plots (not shown) of stars within 7–11 ppm bands, and 17–21 ppm bands from the histogram of Figure 8 the stars appear to be uniformly distributed over the full focal plane. There is a mild dependence on galactic latitude in that noisier stars are
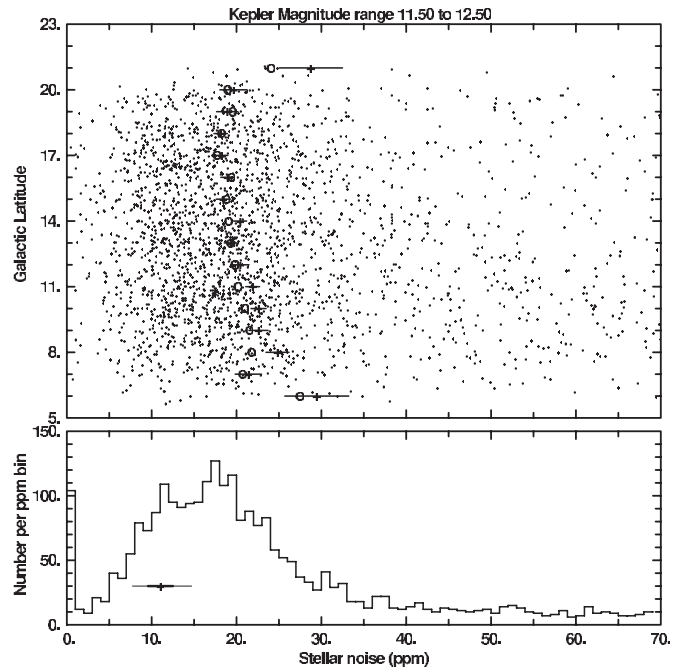

Figure 8. Upper panel shows the intrinsic stellar noise in ppm for the $Kp = 11.5$–12.5 sample as a function of galactic latitude. Medians evaluated up to 100 ppm are shown as "o," while means from up to $3\times$ the median at each degree of galactic latitude are shown as "+" symbols. Standard errors for the means are shown. The lower panel shows a histogram of number of stars per ppm bin. The mean and rms distribution for solar noise levels over quarter-long intervals spanning a solar cycle are shown by the "+" and heavy horizontal line, with the full extent of solar noise per quarter the thin line.

statistically more likely at low galactic latitude: for intrinsic noise of 30–70 ppm 60% are at $b < 13°$, while at 17–21 ppm and 7–11 ppm the fraction drops to 49% and 45%, respectively. The medians (up to 100 ppm) and means (using stars up to $3\times$ median) over all latitudes are 19.6 and 20.3 ± 0.3 ppm, respectively. A more realistic estimate of the errors for the median and means would be to adopt the spread resulting from the range plotted in Figure 7 which yields ± 1.0 and ± 1.3 ppm, respectively.

Representative stars from quiet, moderate, and high noise levels are shown in Figure 9. For the quietest stars the *Kepler* photometry does not definitively show any variability. By the time stars have intrinsic noise levels over 30 ppm it is common to be able to see evidence of what is likely rotational modulation as seen in the bottom panel of Figure 9.

3.6. Consideration of Crowding and Superposition on Noise

We have considered contributions to variations in detected flux arising from Poisson statistics on the source and sky, detector readout noise, separate additive (in variance) terms that vary by quarter, and by detector channel number. After accounting for the above, residual variations have so far been assumed to represent changes inherent to the individual stars.

There are two additional terms that need to be considered, in at least a statistical sense, to discern if the overall decomposition of noise terms is reasonable. Given the large pixel scale of *Kepler* it is common for significant amounts of light within the photometric apertures to arise from nearby neighbors—the amount of this that we know about is referred to as the contamination fraction. By design we have limited stars in our $Kp = 11.5$–12.5 sample to have less than 20% of the light provided by neighboring stars (fewer than 1% of 12th magnitude
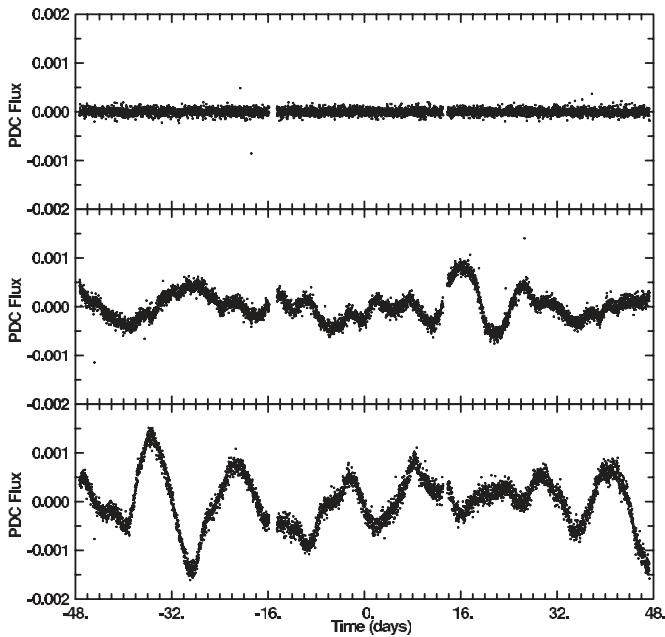
Figure 9. Representative time series for stars from low (5.7 ppm), medium (20.4 ppm), and high (35.0) intrinsic noise levels are shown. From top to bottom these stars are KIC 4662814, KIC 4663537, and KIC 4283320. All of the time series are from Q5 and are the direct pipeline provided PDC fluxes after subtracting out and normalizing by an overall median.

Table 3
Number of Stars per 19.6 *Kepler* Pixel Area

Kp	13.5	14.5	15.5	16.5	17.5	18.5	19.5	20.5	21.5	22.5
$b = 19$	0.008	0.016	0.03	0.04	0.06	0.09	0.12	0.15	0.19	0.21
$b = 13$	0.012	0.025	0.05	0.09	0.14	0.20	0.25	0.33	0.42	0.52
$b = 7$	0.028	0.057	0.12	0.23	0.45	0.78	1.17	1.49	1.78	2.22

Notes. Besancon model star counts (Robin et al. 2003) for average number of background blended star per buffered *Kepler* photometric aperture for 12th magnitude stars.

stars observed by *Kepler* are above this 20% cut). In evaluating the Poisson statistics contribution we have not included this maximum of 20%, average of 2% in the signal, but have allowed for this to be included in the statistical noise. We have not, however, allowed for potential variability of the contaminating stars introducing modulation of the target star flux. In most cases, the DC level of contaminating fluxes is known from relative magnitudes, separations, and assuming a PSF, but the contaminating star will not typically have been observed by *Kepler*. This may be thought of as a "known unknown;" we know the DC component, but not the AC contribution in the combined time series. Of the "unknown unknown" variety there will be a chance that target stars have background stars within the photometric aperture. We will have already accounted for any Poisson statistics provided by such unknown blended stars, but will not have allowed for possible variations in the signal flux provided by these stars.

In both of these cases, we can statistically estimate how much the CDPP and inferred intrinsic stellar noise is likely to be influenced by these added contaminants. We address the issue of blended background stars first. We adopt several assumptions that will, if anything, overestimate the influence of blended background stars.

1. The aperture size, or area on the sky within which to consider statistical blends, is taken to be the actual optimal aperture size with a half-pixel radius buffer. At 12th magnitude this padded aperture averages 19.6 pixels, but is allowed to vary star-by-star and quarter-by-quarter to match actual values used in the pipeline.
2. We adopt the set of all $Kp = 11.5$–12.5 stars that were observed in each of Quarters 2–6 as a set from which to randomly pull time series to be added with appropriate dilution depending upon relative magnitudes. Since red giants are inherently much noisier than dwarfs, and many of these have been dropped (Batalha et al. 2010) from the

planetary target list, we replicated the observed red giants to bring their total fraction up to 50%. This is slightly greater than the 47% red giant fraction implied by the KIC at 12th magnitude, and likely an even greater overrepresentation for much fainter background stars.
3. Star counts as a function of galactic latitude over the *Kepler* field were adopted from the Besancon galactic model (Robin et al. 2003), of which over $Kp = 14$–16 were some 20% larger than an estimate based on the KIC directly at field center. Over the 19.6 pixel aperture the number of stars per magnitude bin was adopted as tabulated in Table 3 for three galactic latitudes.

To simulate the impact of unknown background stars, that if sufficiently variable would increase the apparent variability of the usually much brighter target star, we start with the 69,005 set of time series. For each star the probability of a background star within one magnitude bins over $Kp = 13.5$–22.5 overlapping with the target aperture is assessed. For example at $b = 13°$ there would be a 14% chance of a contributing star at 17.5, and 52% at 22.5, etc. When the random selection probability indicates a contaminating background star should be added, a random draw from the set in number 2 above is made, diluting the added signal as the ratio of brightness of the background bin to the source star. When making this addition the similarly scaled median of the source star is subtracted so that we effectively add in just the variability, and not a zero-point offset in total counts. Only about 10% of $Kp = 12$ stars based on Table 3 would have a star within a δ-magnitude of about 4 contributing, but summed to a δ-magnitude of 10 the number of stars added in averaged about two at field center. When the number of expected stars exceeds unity per magnitude bin a random draw will always be added in with appropriate dilution based on magnitudes, but also scaled back up by the effective number of such stars, e.g., $\times 2.22$ at low galactic latitude and $Kp = 22.5$.

The resulting time series are then run through the same software used to extract the proxy CDPP values, and that is then used to decompose the noise into the several terms discussed earlier. The primary result of allowing for additional blended background stars is shown in Figure 10 where the relative effect on stars having 5–20 ppm from Figure 8 is shown. The majority of originally quiet stars are perturbed by less than 1%, with about 10% increased in inferred noise level by 1%, etc. The fraction of stars originally within the 5–20 ppm domain that moved into the 40–70 ppm range total only 1.5%, and the number fraction from this quiet set moving to greater than 70 ppm is 1.3%. While not entirely negligible, the impact of allowing for variable background stars is minor. The number of stars promoted to the 40–70, and greater than 70 ppm domains is about 10% of the number of stars observed to be this noisy. The overall increase of median and mean noise evaluated as in Section 3.5 is only 0.2 and 0.1 ppm.
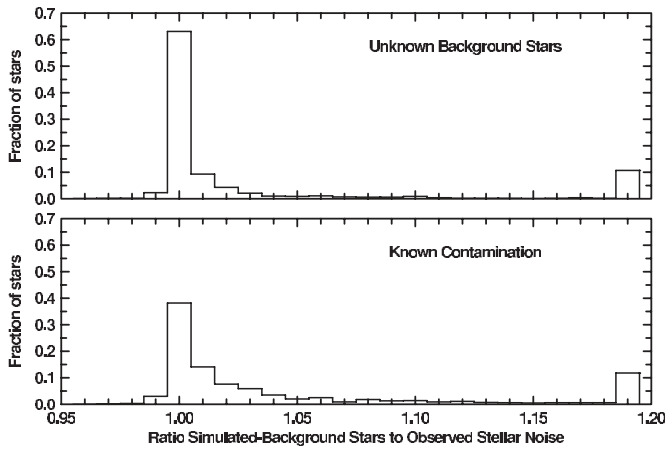
Figure 10. Upper panel shows the ratio of inferred noise levels for stars originally within 5–20 ppm noise levels to the results from adding simulated (unknown) background variable stars. The final bin includes all values out of range. The lower panel shows the same for the simulations taking into account that known blended stars may be variable.

The second consideration is to assess by how much the known levels of contamination are likely to contribute for formal estimates of intrinsic stellar noise. For each star we take the maximum contamination (fraction of light within optimal aperture contributed by known neighbors) over Quarters 2–6 for the $Kp = 11.5$–12.5 sample, the mean of this is 0.021. Using a similar approach as for the background stars, we take the contamination fraction as the dilution factor (adjusted as well for the relative brightness of target and randomly drawn perturber), and always add in one randomly drawn additive star. The results are shown in Figure 10, again as the relative impact on stars that were within 5–20 ppm intrinsic noise before this. A larger fraction of stars are moved to slightly higher noise levels than was the case accounting for background stars. However, as measured by the number promoted from the 5–20 ppm bin into, or beyond the 40–70 ppm range the fractions remain very modest at 0.9% and 1.2%, respectively. The fractions of stars at high noise levels seem perturbed by about 10% after considering the effects of known contaminating stars and allowing for the fact that some of these will be significantly variable. The overall increase of medians and mean relative to the base from Section 3.5 is again negligible.

The estimates in this section cannot be used to correct inferred stellar noise levels on a star-by-star basis, but do indicate that the impact of either known contaminating stars, or fainter, blended background variables is a statistically minor factor overall. Summaries here and in Figure 10 have considered only statistically average responses over all channels, and at all galactic latitudes.

The equivalent of Figure 10 drawn for only low galactic latitudes would show somewhat larger responses. We quantify this by evaluating the slope of the mean values over 1° steps for $b = 8$–18 for the equivalent of Figure 8 for these simulations. The direct observations have a slope of -0.58 ppm deg^{-1}, while the background and contamination simulations come in at -0.81 and -0.67, respectively. Combined, the excess slope from these simulations is -0.32 ppm deg^{-1}, suggesting that about half the apparent galactic latitude dependence may result from contamination effects. Residual evidence for intrinsic stellar variability dependence on galactic latitude is weak. We will return to these higher order considerations in Section 3.8.

Table 4
Global Roll Up of Noise Terms

Component	Variance (ppm^2)	Noise (ppm)	Baseline Noise (ppm)
Intrinsic stellar	380.5	19.5	10.0
Poisson + readout	283.0	16.8	14.1
Intrinsic detector	116.2	10.8	10.0
Quarter dependent	60.1	7.8	. . .
Total	839.8	29.0	20.0

Notes. The Q2–Q6 variance (and derived noise) contributions for the $Kp = 11.5$–12.5 stellar sample discussed at length in the text. For the baseline, design noise terms, the readout noise is accounted within the intrinsic detector term.

3.7. Overall Noise Decomposition Results

Having now derived noise terms covering contributions that change in time unique to each quarter, that arise from the detector channels, assigned Poisson and readout noise, and intrinsic stellar noise, we may now examine this from a global perspective. In particular, what is the ordering of terms and how do these compare with expectations? If we now put the decomposed terms back together is the CDPP effectively reproduced?

Table 4 provides the four independent variance terms into which we have decomposed the observed variance (CDPP^2). The largest of these is the intrinsic stellar variability for which our value is 19.5 ppm. The budget for stellar variability had been set to 10 ppm (Jenkins 2002); since this term is both the largest contributor overall, and twice the budgeted value, this term strongly deviates from expectations in a significant way. The largest contributor to higher than expected CDPP is an intrinsic stellar variability significantly above expectations. The second largest term at 16.8 ppm includes contributions from Poisson noise on the target star itself, and much smaller contributions from Poisson noise of the sky, and detector readout noise. The mean Kp of this 11.5–12.5 sample of stars is 12.10, and the irreducible terms for Poisson noise and readout are entirely consistent with expectations. The third largest term at 10.8 ppm is a global average (as variances) over the 84 detector channels. Since the detector noise contribution is well below the level of Poisson noise this has little influence on the bottom-line CDPP. Expectations were that a large number of imperfections in the electronics would combine to provide several ppm of equivalent noise, so what we find is broadly consistent with expectations, albeit marginally higher. Finally, the quarter-to-quarter component of noise comes in at 7.8 ppm. This had not been explicitly budgeted for in CDPP estimates, and this term is dominated by Q2 and Q3 which both had excess noise from safing events, telescope repointing, and minor heater cycle/guiding issues that have since been brought under control. Averaged over Qs 4–6 this time-dependent term would be under 5 ppm.

The final line of Table 4 shows the sum of the four variance terms and derived overall CDPP for the $Kp = 11.5$–12.5 sample at 29.0 ppm. This is quite consistent, as it must be unless an inconsistency had arisen with the decompositions with a consistently derived CDPP value for the same stars. This value is 50% larger than the target of 20 ppm. Had intrinsic stellar variations held to 10 ppm for a large fraction of the stars, instead of adopting a broad distribution extending beyond 20 ppm, then the noise roll up would be at 23.6 ppm. (Part of this would be accounted for by our sample mean magnitude being

Figure 11. This shows the distribution of noise intrinsic to each detector channel derived as in Sections 3.2 and 3.4. Solutions are in variance space, translated to equivalent noise by taking a square root. Where the variance, due to inherent scatter in derivation, is negative, the noise is evaluated as minus the square root of the negative of this variance.

Figure 12. By-channel intrinsic variance levels are plotted against by-channel focus as represented by the fraction of total energy in the central pixel for a star centered on a pixel. As expected now for *Kepler*, but contrary to common knowledge, the best photometry is returned for the sharpest PSF channels, even when the PSF is severely undersampled. Channels overplotted with a small circle represent nine cases independently identified to have moderate Moiré pattern noise, and the ten cases with strong Moiré noise have doubled circles added.

fainter than 12.0. A caution applies, though, that scalings in either magnitude, or time do not have precisely the simple form expected due to a varying number of pixels as a function of magnitude and the stellar noise being red, respectively.) Without the higher intrinsic stellar variability we are some 10% above the requirement of 20 ppm CDPP at $Kp = 12$, with the higher intrinsic noise from stars factored in we are some 50% above our noise requirement.

3.8. Detector Noise by Channel and Focus Dependence

It is now instructive to document the inferred excess noise by channel and the dependence of this excess on the instrument focus, which varies significantly over the focal plane. Figure 11 is in the same style as Figure 1 and shows the excess noise level as derived following the steps in Sections 3.2 and 3.4 above. As argued in Table 4 the overall contribution of this excess channel noise is rather modest for the CDPP error budget. Nonetheless it is interesting to note that patterns in this noise exist and seek at least a correlative explanation.

Figure 12 shows the intrinsic excess variance by channel plotted versus the fractional central pixel energy content for a star centered on a pixel for that channel. The straight line is a simple least-squares fit of variance with the focus proxy, assuming no error in the latter. The linear correlation coefficient of excess variance with focus is 0.63, with a sign that clearly indicates the better photometry follows from channels with best focus. This is true even when the resulting PSFs are severely undersampled. As argued in Section 2 the exquisitely good guiding provided by *Kepler* supports excellent photometry even for sharp PSFs; indeed it does best in this circumstance. This convincingly argues that there is no significant effect from intra-pixel sensitivity variations coupled with jitter.

In Section 3.6, we demonstrated that the large *Kepler* apertures, which will lead to blended background (or foreground) stars, do not lead to significantly changed overall noise statistics

when these blends are simulated. For a channel with soft focus (low focus values in Figure 12), larger apertures are used to capture the target flux. This will lead to both larger values for the known contamination from nearby neighbors on the sky, and higher probabilities that unknown blended objects are within the aperture. Using the simulations performed in Section 3.6 we have independently produced versions (not shown) of Figure 12 for both the known and unknown background contaminating cases. In both instances the gross features of Figure 12 are well preserved, although in both cases the slope of channel variance with focus increased by about 10%. This implies that some 20% of the implied channel noise dependence on focus results from the inclusion of more variable stars in poor focus channel apertures. (There is some double counting between the known and unknown simulations, but since the perturbation for both combined remains small we have not attempted to quantify this.)

Further support for the reasonableness of the noise decomposition comes through comparison of entries in Figure 12 for channels showing Moiré patterns in the background based on ground-based, and Q0–Q1 data analyses (Caldwell et al. 2011; Kolodziejczak et al. 2010). Of the ten channels having worst Moiré features, eight of these fall above the linear fit with a mean offset of 72 and standard error of 21 ppm^2—a significance of over 3σ. Seven of nine channels flagged independently as moderate in their Moiré features are above the linear fit, but the mean offset drops to 28 ± 31 ppm^2. Four of the five channels with largest excess noise in Figure 12, either in absolute terms, or relative to the linear fit correspond to those flagged for Moiré influence. The Moiré pattern noise is thought to arise from temperature-sensitive operational amplifiers used extensively in the video chain electronics, which may show subtle layout-dependent instability when used at the low gains adopted for *Kepler*. The oscillation's frequency range, rate of

Table 5
Percentage of Quiet and Noisy Bright Stars

Spectral type	A0	A5	F0	F5	G0	G5	K0	K5	M0
Central T (K)	10700	8250	7375	6550	5925	5575	5075	4325	3625
% at < 10 ppm	20.5	10.9	5.9	0.7	0.0	1.2	5.4	0.0	0.0
% at > 50 ppm	39.8	39.0	72.6	82.3	30.3	23.8	40.6	76.0	92.9
No. of stars	88	46	51	305	267	84	74	24	14

Notes. Effective temperature divisions between bins are at 8900, 7800, 6950, 6150, 5700, 5450, 4700, and 3950 K, with A0 extending to 12,500 K, and M0 to 3300 K. Number of stars is the total count per spectral bin.

change, and pattern among the channels matched closely those characteristics in the dark images, strongly suggesting that the artifact follows from sampling the >1 GHz amplifier oscillation at the 3 MHz serial clocking rate. Since the effect is temperature sensitive the pattern will drift in time, and the relative importance of the imposed Moiré pattern noise will be different quarter-to-quarter for the channels sensitive to this.

Having shown that some quarters (Q2 in particular), and channels are noisier than others we tried creating a new version of Figure 5 in which only the best Quarters, Q4–Q6, and the lowest noise (29 of 84) channels were allowed to contribute. The resulting figure was very similar to Figure 5. The values going into Figure 5 were based on means over all quarters, but without using the maximum (usually Q2). The excess variance contributed by the worst channels on the instrument remain below the level of intrinsic stellar noise, and only comparable to Poisson contributions as detailed in Table 4. Thus the CDPP shown in Figure 5 is considered robust.

3.9. Stellar Correlations with Effective Temperature

At the suggestion of the referee we have explored the hypothesis that stars of spectral type A to early F with insignificant surface convection zones should frequently be low noise. This is pursued in the spirit of a sanity check on the primary conclusions of this paper, namely that solar-type stars are typically noisy (where by *Kepler* standards this means 20 ppm on timescales of 6.5 hr). To simplify interpretations we tabulate the fraction of stars in spectral-type bins spanning A0, A5, ..., M0 that have noise levels (CDPP) less than 10 ppm for stars with $Kp = 7$–11 where Poisson noise contributions allow such low values if the stars are inherently quiet, and if the instrument is not adding significant noise. All known eclipsing binaries and planet transit hosts have been excluded to avoid cases with spuriously high CDPP from non-stellar events. We also show in Table 5 what fractions of stars within these bins are quite variable at greater than 50 ppm. The requirement is that these limits be met in at least two of Quarters 3–6, and generally there is excellent consistency across quarters for either quiet or noisy stars.

The primary hypothesis is well satisfied: a significant fraction of early-type stars do have noise levels that are low compared to those that occur for solar-type stars. In particular, this may be taken as support that *Kepler* itself does not impose a floor to the noise levels, at least not at a level generally relevant to CDPP for 12th magnitude stars. When the Poisson term is forced low by selecting bright stars, and stars are inherently quiet, *Kepler* returns low noise levels. There are clearly trends in the distribution of both quiet and noisy stars with spectral type that call out for further astrophysical interpretation, this is beyond the scope of this paper. Here, we merely note that A to early-F stars do show frequent very low noise levels, in stark contrast
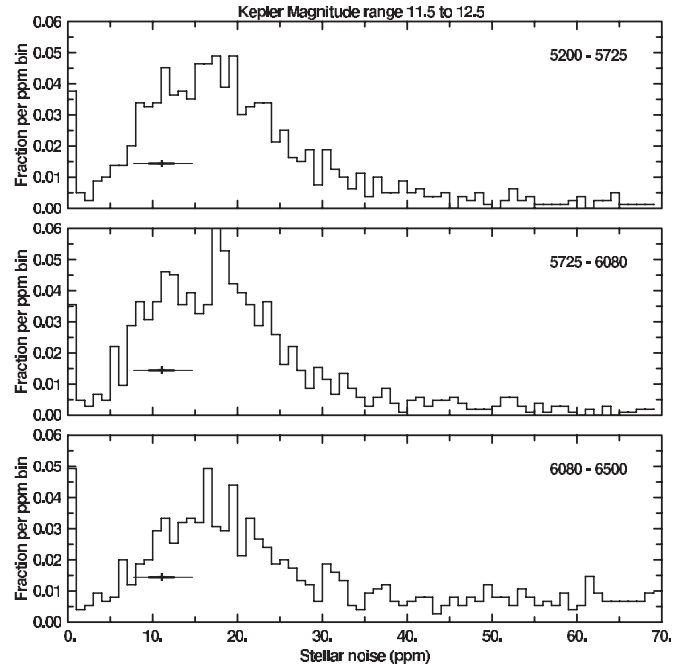

Figure 13. Histogram shown in Figure 8 is here split into equal thirds of cool (from top) to warm stars. Over the primary range of solar-type stars relative differences are subtle with the most noticeable feature a more pronounced tail to higher values for warm stars.

to the absence of such quiet stars in the solar type regime (with a possible small subset of quiet stars near K0). Balancing this, though, the fraction of stars that are really noisy as measured by our cut at > 50 ppm reaches a distinct minimum for solar-type stars. The small sample size and potential for contamination by misclassified giants as dwarfs suggest caution should be exercised in interpreting the K5 and M0 bins of Table 5.

The distribution of intrinsic stellar noise within our primary range of 5200–6500 K is shown in Figure 13. The primary difference noticeable over this temperature range is a higher tail of moderately variable stars for the earlier spectral type.

4. SIMULATION OF STELLAR NOISE

We estimated the properties of the stellar population observed by *Kepler* using the code TRILEGAL (Girardi et al. 2000), which is designed to simulate photometric surveys in the Galaxy. A synthetic population of solar-type stars was extracted for the *Kepler* field of view by applying the same selection cuts as were applied to the real stars. From the properties of each solar-type star we then estimated the stellar contribution to its CDPP, using the procedures outlined in Section 4.2 below. Before discussing these procedures, we begin with a brief description of TRILEGAL.

4.1. Galactic Population Synthesis Models

In TRILEGAL, several model parameters (such as the star formation history and the morphology of different galactic components) were calibrated to fit Hipparcos data for the immediate solar neighborhood (Perryman et al. 1997), as well as star counts from a wide area (with 2MASS; Cutri et al. 2003), and a few deep photometric surveys, i.e., CDFS (Arnouts et al. 2001), and DMS (Osmer et al. 1998). We adopted the standard parameters describing the components of the Galaxy and simulated the stellar population in the sky area observed in each of the 21 five-square-degree *Kepler* sub-fields of view, considering for each of them an average interstellar extinction at infinity (Schlegel et al. 1998). The extinction is assumed to be caused by an exponential dust layer with a scale height above and below the galactic plane, equal to 110 pc. The photometry in TRILEGAL was simulated with the known wavelength response function of *Kepler*, and the synthetic population was magnitude-selected, using the same range as the observed sample.

4.2. Estimation of Stellar Noise

The stellar noise was assumed to have two components: one due to activity and another due to granulation. It was assumed that any significant contribution from p-mode oscillations would have been removed by the strong bandpass filtering implicit in construction of the CDPP (see below). Empirical scaling relations were used to predict parameters describing the activity and granulation, which in turn were used to estimate the underlying power spectral density (PSD; as a function of cyclic frequency ν) due to each contribution. We assumed that the contributions could be described as exponentially decaying functions in time parameterized by an rms amplitude, σ, and a timescale, τ. The underlying PSD is a zero-frequency-centered Lorentzian of the form (Harvey 1985)

$$\mathrm{PSD}(\nu) = \frac{2\sigma^2\tau}{1 + (2\pi\nu\tau)^2}, \qquad (2)$$

with the variance in the time domain being equal to $\sigma^2/2$. We discuss the validity of using this function in Sections 4.2.1 and 4.2.2 below.

Frequency spectra were constructed by adding the PSD due to activity and granulation. Spectra were computed at the natural frequency resolution of each of the 3 month long quarters of *Kepler* observations (i.e., $\simeq 0.13\,\mu$Hz), up to the Nyquist frequency for 29.4 minute LC observations. They were then multiplied by two functions to allow for the bandpass filtering inherent in construction of the CDPP. The first function described the high-pass filtering given by application of the 2 day Savitsky–Golay filter. Its filter response is plotted in Figure 14 as the black line. The second function (sinc-squared) described the low-pass filtering given by averaging of data into 6.5 hr blocks, i.e., $\mathrm{sinc}(\pi\nu T_{av})^2$, with $T_{av} = 6.5$ hr. Its filter response is plotted in Figure 14 as the gray line.

The variance (CDPP squared) was then estimated from the sum of the PSD in the frequency spectrum, multiplied by the natural frequency resolution (i.e., by invoking Parseval's theorem which demonstrates that the total power in a signal is the same if computed in the time domain or in the Fourier transform frequency domain, see Press et al. 1992). The normalization between the time and frequency domains was double-checked using artificial time-series data.

The TRILEGAL simulations provide independent stellar parameters for the $\approx$50% of cases it returns as physical binaries.
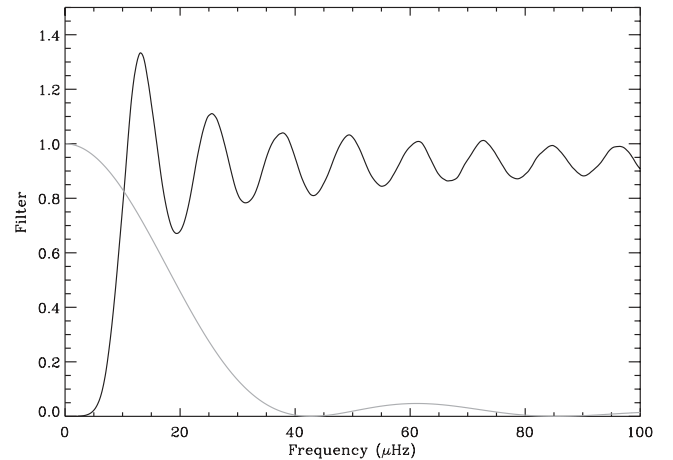

Figure 14. Filter response due to 2 day Savitsky–Golay filter (black line); averaging of data from 29.4 minutes to 6.5 hr cadence (gray line). A frequency of 11.6 μHz corresponds to 1 day.

We assume that all such binaries will be unresolved by *Kepler* and treat each binary as one star for which to report noise. The individual rms fluctuations for each component of binaries are reduced by the sum of the individual fluxes and then recombined in variance space to provide the final noise level.

As argued in Section 3.6 the real observations suffer from small increases of noise due to superposition of sources which are themselves variable. We allow for this relatively minor correction by adopting the contamination factors used for Figure 10. An underlying probability distribution for the noise multiplication factors (due to both the known contamination and unknown background stars) is formed, then for each star in the simulation a random number is generated and used to fix the multipliers (i.e., to map the random numbers onto the underlying distribution). Thus some 25% of stars have noise levels boosted by 1%, with about 80% of stars having noise levels increased by less than 20%.

4.2.1. Description of Activity

We assume that the rms amplitude of the activity signal, σ_{act}, may be estimated from predictions of the Ca H and K emission index, R'_{HK}. We adopt empirical scaling relations in the literature—which use as input the fundamental properties of the synthetic stars—to estimate the rotation period, P_{rot}, and the convective turnover time, τ_{con}, at the base of the convective envelope, from which the R'_{HK} are predicted from the Rossby number $Ro = P_{rot}/\tau_{con}$.

We estimate the P_{rot} of the stars using the empirical relationship of Aigrain et al. (2004), which was derived from analysis of photometric data taken on stars in the Hyades (Radick et al. 1987, 1995). The relationship uses the $B - V$ color and the age, T, of each star as input, and assumes a $t^{0.5}$ spin-down in the periods (Skumanich 1972). We also tested the empirical relationship of Cardini & Cassatella (2007), which takes the mass M and age T, with the spin-down calibrated to go like $t^{0.45}$. The convective turnover time, τ_{con}, was estimated from the empirical relationship of Noyes et al. (1984), using the $B - V$ color as input. Mamajek & Hillenbrand (2008) discuss how this relationship provides a reasonable match to recent computational predictions based on either mixing-length theory or full turbulence spectrum treatments of convection. To go from $Ro = P_{rot}/\tau_{con}$ to R'_{HK} we used the empirical relationship of

Noyes et al. ([1984](#)). We also tested the empirical relationship of Mamajek & Hillenbrand ([2008](#)).

The final step takes us from R'_{HK} to σ_{act}. Data on rms variations observed in solar-type stars and their relation to the observed R'_{HK} are presented in Radick et al. ([1998](#)), Lockwood et al. ([2007](#)), and Hall et al. ([2009](#)). These data suggest a power-law dependence of the form $\sigma_{act} \propto (R'_{HK})^{1.75}$, with the observed rms variation for the Sun being about 500 ppm. As will be noted further below, the ground-based data generally pertain to timescales of weeks, while we are considering timescales of several hours.

To check the calibration, we analyzed around 12 yr of photometric "Sun-as-a-star" observations (used also in Section [3.3](#)) made in the green wavelength channel of the VIRGO/SPM instrument onboard the ESA/NASA *SOHO* spacecraft (Fröhlich et al. [1997](#)). The stellar observations referred to above were made in Strömgren *b* and *y*, and should have a similar response to the narrowband green SPM data. We divided the 12 yr SPM light curve into contiguous 3 month data sets—corresponding to the quarter-long *Kepler* data sets—and then reduced the cadence in each data set from 60 s to 30 minutes (by averaging into 30 datum blocks). The rms variation due to stellar activity was then estimated (the estimated contribution from granulation having first been removed; see Section [4.2.2](#) below). The estimated $\sigma_{act, \odot}$ varied from about 150 ppm at solar activity minimum to just over 600 ppm at solar activity maximum, with an average value of around 350 ppm. This average differs from the 500 ppm solar value returned by the ground-based stellar observations, which may reflect the impact of different averaging lengths for the data (a point we return to below, just after Equation ([4](#))). We therefore apply a multiplicative correction of $(350/500) = 0.7$ to the empirical scalings suggested by the stellar data.

Two further corrections are applied. First, we make a multiplicative correction of $\simeq 0.8$ to allow for the fact that the *Kepler* bandpass has significant width in wavelength resulting in a redder mean response by 20% compared to the narrowband green SPM channel (see Section [3.3](#) above).

Second, we correct for the impact of the angles of inclination offered by the stars. As discussed in Knaack et al. ([2001](#)), as the angle of inclination is decreased from 90° to the most probable case of 57° so variations due to photometry will increase and those due to Ca H and K emission will decrease. Knaack et al. ([2001](#)) modeled the expected changes for a Sun-like star and predicted that the aforementioned decrease in angle would lead to a $\approx 5\%$ increase in irradiance variability (the *Kepler* wavelength response is much closer to the irradiance response than it is to the Strömgren *b* and *y* response[12]). Knaack et al. predict a negligible decrease in the absolute Ca H and K flux ($\approx 1\%$, a change which we choose to ignore here). The solar data come from observations where the angle of inclination offered by the Sun is close to 90°. To correct the calibration to the most probable angle of 57°, we therefore multiply the average $\sigma_{act, \odot}$ inferred from analysis of the solar data by the factor 1.05.

The stellar data presented in Hall et al. ([2009](#)) follow:

$$\sigma_{act} \simeq 10^{(11.5+1.75 \, \log_{10} R'_{HK})} \text{ ppm.} \quad (3)$$

Application of the multiplicative corrections (combined factor of $\simeq 0.6$) gives our adopted empirical relation:

$$\sigma_{act} \simeq 6 \times 10^{(10.5+1.75 \, \log_{10} R'_{HK})} \text{ ppm.} \quad (4)$$

Implicit in our adoption of the above is that the exponent of the power-law dependence (here, 1.75) does not change when the data are averaged on different timescales, i.e., the temporal coverage of the ground-based stellar observations is such that their data provide variability information on timescales of several months to years, while (in the absence of any other stellar reference) we have used these data to calibrate changes on much shorter timescales. We have not included any perturbations to Equation ([4](#)) to allow for the fact that we will be catching different stars in different phases of their stellar cycles, assuming instead that the impact of this variability will tend to average out over the ensemble.

With regards to the timescale of the activity, τ_{act}, we make the gross approximation of applying the solar timescale to all synthetic stars. Analysis of the green SPM channel data returned an estimate of $\tau_{act, \odot} \simeq 8$ days, with the observed PSD showing a reasonable match to the Lorentzian form of Equation ([2](#)). This timescale of course differs from the solar rotation period of $\simeq 26$ days, and reflects the complicated interplay between rotational modulation and the lifetimes of active regions on a timescale (3 months) that captures only three rotation periods. Aigrain et al. ([2004](#)) suggested that the rotational timescale may become dominant in more rapid rotators. We therefore tested the impact of setting $\tau_{act} = P_{rot}$ when $P_{rot} \lesssim 8$ days, but found that this did not have a significant impact on the distribution of predicted stellar noise values.

4.2.2. Description of Granulation

We follow Huber et al. ([2009](#)) and Chaplin et al. ([2011b](#)) in assuming that the timescale for the granulation, τ_{gran}, scales inversely with the frequency of maximum oscillations power, ν_{max}, as proposed by Kjeldsen & Bedding ([2011](#)). To fix the rms of the granulation, σ_{gran}, we follow the procedure outlined in Chaplin et al. ([2011b](#)). This procedure assumes that the typical size of a convective granule is proportional to the scale height for an isothermal atmosphere, and that all granules behave in a statistically independent manner so that the total rms fluctuation scales inversely as the square root of the number of observed granules (e.g., Schwarzschild [1975](#); Kjeldsen & Bedding [2011](#)). This leads to $\sigma_{gran} \propto \nu_{max}^{-0.5}$.

In order to fix solar values for τ_{gran} and σ_{gran}, we again analyzed the green SPM channel Sun-as-a-star data. Fits to the PSD in the frequency region below the solar *p* modes where the granulation dominates gave average values of $\tau_{gran, \odot} = 220$ s and $\sigma_{gran, \odot} = 75$ ppm. Since $\nu_{max} \propto MR^{-2}T_{eff}^{-0.5}$ (Kjeldsen & Bedding [1995](#); Chaplin et al. [2008](#)), the scaling relations we adopt to estimate τ_{gran} and σ_{gran} are then given by

$$\tau_{gran} = 220 \left(\frac{M}{M_\odot}\right)^{-1} \left(\frac{R}{R_\odot}\right)^2 \left(\frac{T_{eff}}{T_{eff, \odot}}\right)^{0.5} \text{ s,} \quad (5)$$

and

$$\sigma_{gran} = 75 \left(\frac{M}{M_\odot}\right)^{-0.5} \left(\frac{R}{R_\odot}\right) \left(\frac{T_{eff}}{T_{eff, \odot}}\right)^{0.25} \text{ ppm,} \quad (6)$$

with $T_{eff, \odot} = 5777$ K. Use of the zero-frequency-centered Lorentzian (Equation ([2](#))) to describe the granulation provides a

---

[12] As already noted in the text, a multiplicative factor of 0.8 corrects for the *Kepler* response being redder than the VIRGO/SPM green or Stromgren *b* + *y* bands. Analysis of total solar irradiance data collected by the PMO6 instrument on VIRGO/*SOHO* gives values for rms variability that are also about 0.8 times the VIRGO/SPM green-band variability.
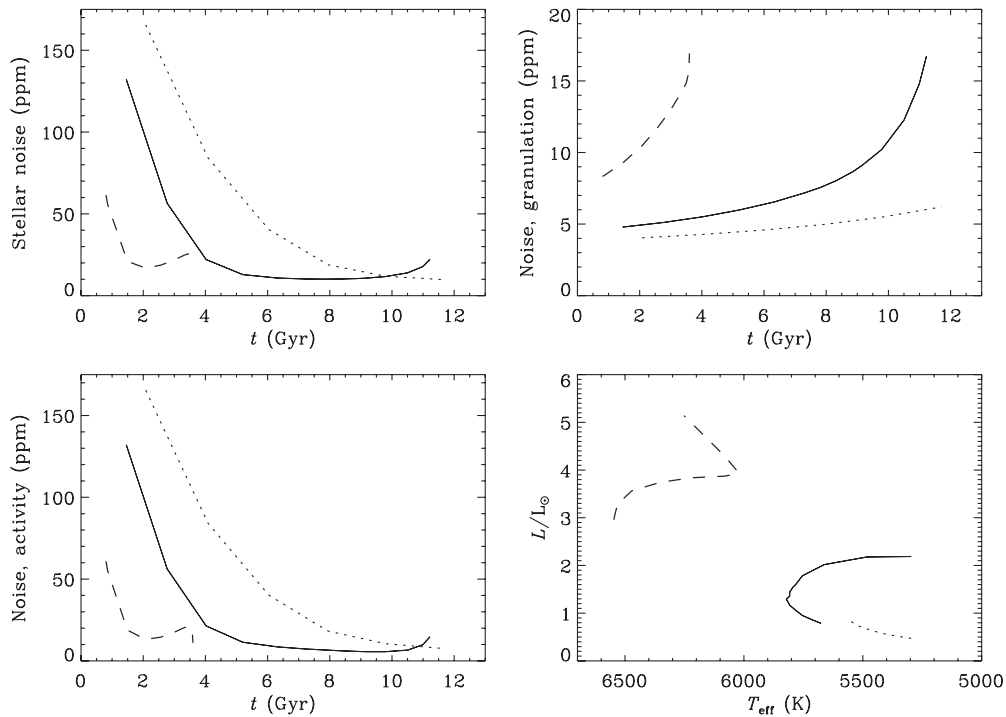
Figure 15. Simulated total stellar noise on 6.5 hr timescales (top left-hand panel) and noise due to granulation (top right-hand panel) and activity (bottom left-hand panel) vs. time, t, for three models of mass 0.9 $M_\odot$ (dotted lines), 1.0 $M_\odot$ (solid lines), and 1.3 $M_\odot$ (dashed lines). The bottom right-hand panel shows the models on an HR diagram.

reasonable description of the observed PSD at frequencies below the range occupied by the p modes. The Lorentzian description does however appear to fail at higher frequencies (e.g., see Huber et al. 2009; Karoff 2011), which is not a cause for concern here since the band-limited filtering used to construct the CDPP selects out PSD only at very low frequencies (see Section 4.2 above).

Figure 15 plots the simulated total stellar noise (top left-hand panel) and noise due to granulation (top right-hand panel) and activity (bottom left-hand panel) versus time, t, for three models of mass 0.9 $M_\odot$ (dotted lines), 1.0 $M_\odot$ (solid lines), and 1.3 $M_\odot$ (dashed lines). The bottom right-hand panel shows the models on an HR diagram. As the stars get older the contribution from granulation increases, while that from activity declines until the stars leave the main sequence. At this point the shift to lower effective temperature increases the convective turnover time, τ_{con}, thereby increasing the Rossby number, Ro, thus halting and even reversing the decline of activity with age (Gilliland 1985). Our exclusion of subgiants from the stellar sample prevents the latter effect from being significant here.

4.3. Results from Synthetic Population

Figure 16 plots the estimated full CDPP of the solar-type stars in the synthetic population. To give the full CDPP, we added (in variance space) a contribution to represent shot noise which was calibrated on a linear interpolation (random on [0,1] by star) of the minimal LC noise and upper envelope noise models presented in Jenkins et al. (2010b). Figure 17 shows the respective contributions from activity (left-hand panel) and granulation (right-hand panel). The synthetic plot shows the key features present in the CDPP plot of the real data (Figure 4): a concentration of stars which map the domain just above the lower-bound defined by the shot noise limit, and a wider spread of stars at higher CDPP. The concentration is less well defined
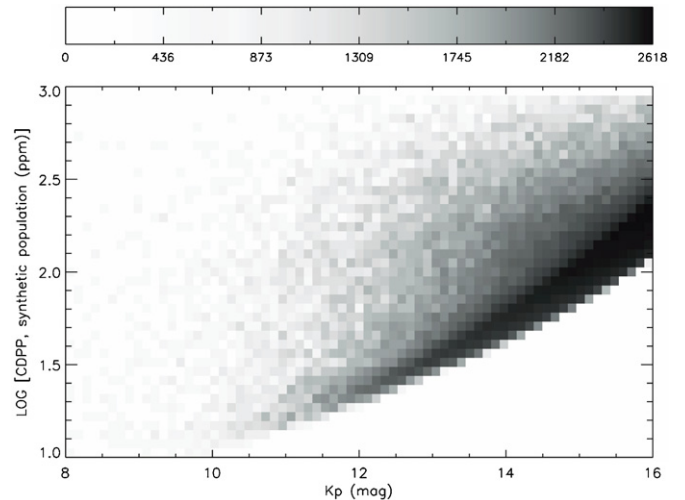

Figure 16. Estimated full CDPP of the synthetic population of solar-type stars. The bar at the top defines density of stars per 0.1 (mag) × 0.05 (log CDPP) bin.

in the synthetic plot and appears to widen slightly at fainter apparent magnitudes.

The predicted contribution from granulation is plotted in the right-hand panel of Figure 17. The lower swathe of stars maps the granulation of either single stars or the primary components of binaries, and is strongly band-limited by the filtering inherent in construction of the CDPP. The strong, lower concentration to granularity is evidently in part responsible for the pile-up of values near 8–12 ppm in the synthetic stellar noise plot, which suggests a similar contribution for the real data. The second swathe at higher noise maps the extra contribution from the secondary components of binaries.

Figure 18 is analogous to Figure 8 and shows the distribution of stellar noise for solar-type stars in the synthetic population
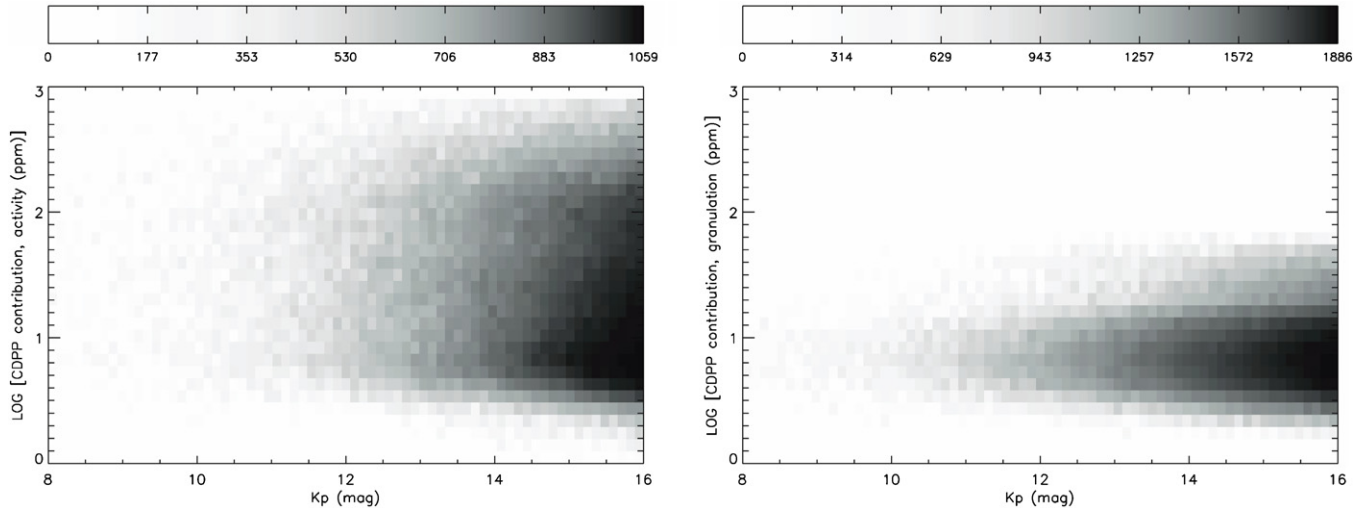
Figure 17. Left-hand panel: contribution from activity to CDPP of solar-type stars in synthetic population. Right-hand panel: contribution from granulation. Bars at the top define the density of stars per 0.1 (mag) × 0.1 (log CDPP) bin.
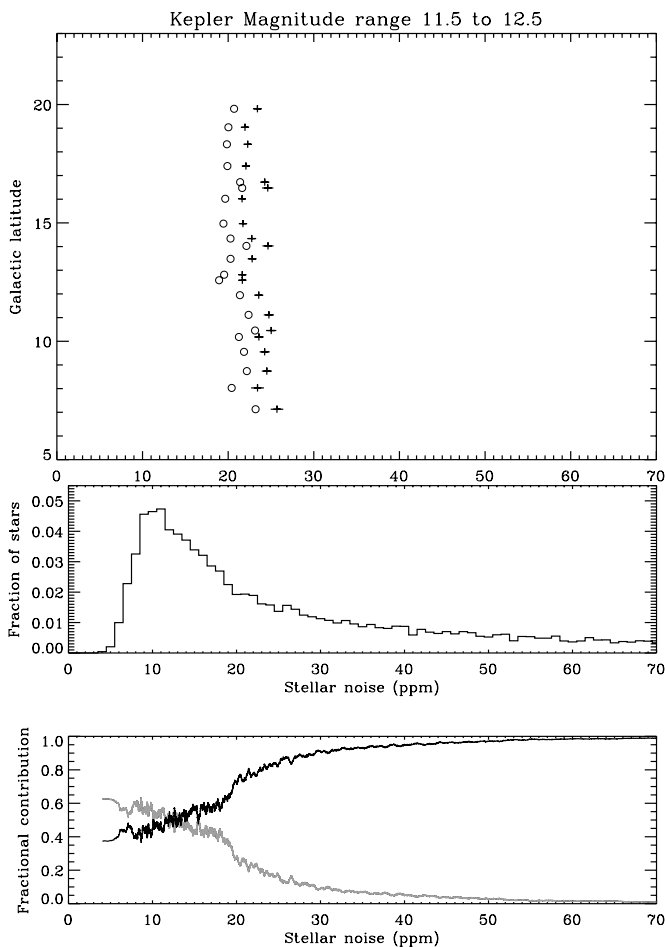

Figure 18. Distribution of stellar noise for solar-type stars in the synthetic population having *Kepler* apparent magnitudes in the range 11.5 to 12.5. Top panel: Mean (with error bars) and median (open circles) stellar noise levels, computed as per the real data in Figure 8. Middle panel: Distribution of stellar noise. Bottom panel: Relative contributions in variance space of granulation (gray line) and activity (black line).

having *Kepler* apparent magnitudes in the range 11.5–12.5. The mean and median stellar noise levels plotted in the top panel

were computed as per the real data. This is the result of averaging over 10 independent realizations of TRILEGAL simulations.

The synthetic stellar noise shows less variation with galactic latitude, *b*, than does the real data (recall the latter display a slight decrease in noise with increasing *b*). For intrinsic noise of 30–70 ppm 46% of the artificial stars lie at $b < 13°$, while at 17–21 ppm and 7–11 ppm the fraction drops only marginally to 43%.

The histogram in the middle panel of Figure 18 bears some similarity to the histogram of the real data in Figure 8, with a common lower envelope and an extended tail. The distribution of stars is strongly peaked toward the lower end of the plotted noise range, although the synthetic population is peaked at a lower absolute noise than the real population. This minor difference in absolute scale is within a reasonable range of uncertainty for either the simulations, or the noise decomposition of real data. We note that the bi-modal signature seen in the real data is not present when we average results from independent realizations of the population synthesis, and therefore the bi-modality is not well established in either the simulated or real data. Both the simulations and decomposition robustly support the existence of a broad distribution of intrinsic stellar noise over ~10–20 ppm near $Kp = 12$. The medians and mean over all galactic latitudes computed as for the real data in Section 3.5 are 21.6 and 23.7 ppm, respectively. Although more peaked at low values, the global statistics average some 15% higher than the observations.

The bottom panel of Figure 18 shows the relative contributions in variance space of granulation (gray line) and activity (dark line). The respective fractional contributions are quite similar at low stellar noise; at high noise, it is the activity which clearly dominates.

As noted previously, we also tested the impact on the predicted stellar noise of the use of different empirical scaling relations in estimation of the activity component. Rotation periods predicted with the relation of Cardini & Cassatella (2007) show reasonable agreement with our adopted relation of Aigrain et al. (2004), although the agreement worsens progressively for masses above 1.3 $M_\odot$ (the Cardini & Cassatella (2007) relation is calibrated for lower masses). When we restrict to synthetic stars in the range $M < 1.3\,M_\odot$, the distributions of estimated stellar noise are quite similar in appearance, although the peak
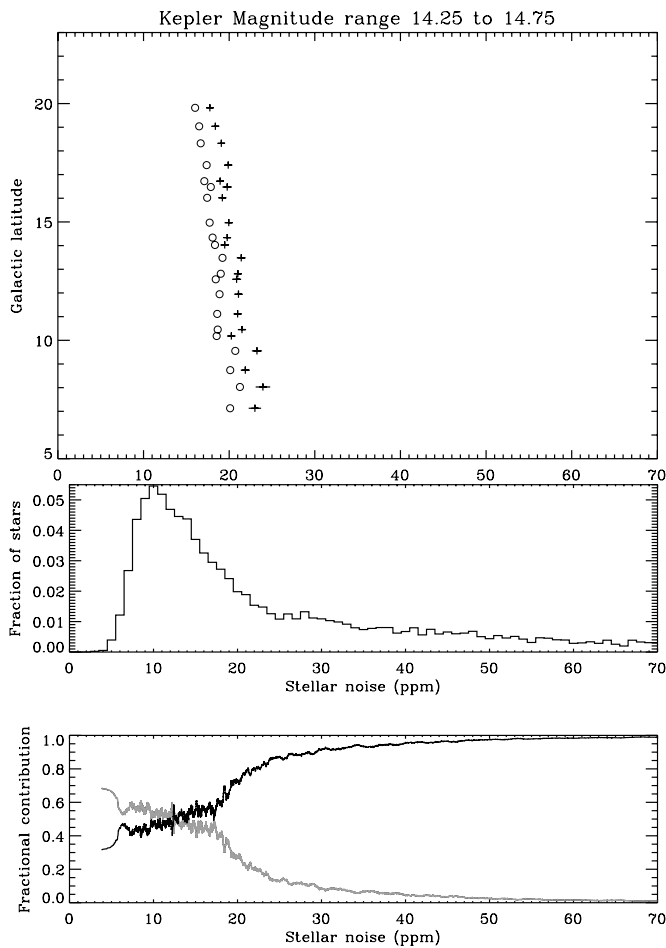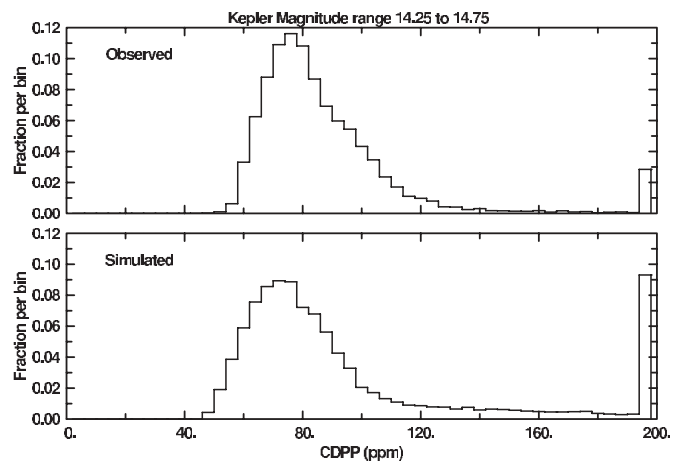
Figure 20. Upper panel shows distribution of observed CDPP for the $Kp = 14.25$–14.75 sample. The lower panel shows the distribution of simulated CDPP for the same magnitude range drawn from Figure 16.

Figure 19. Distribution of stellar noise for solar-type stars in the synthetic population having *Kepler* apparent magnitudes in the range 14.25–14.75. Top panel: mean (with error bars) and median (open circles) stellar noise levels, computed as per the real data in Figure 8. Middle panel: distribution of stellar noise. Bottom panel: relative contributions in variance space of granulation (gray line) and activity (black line).

in Figure 18 is shifted to a slightly lower noise when the Cardini & Cassatella (2007) relation is used, as it gives slightly longer rotation periods (on average).

Our adopted relation to convert from Ro to R'_{HK} (Noyes et al. 1984) and the corresponding relation given in Mamajek & Hillenbrand (2008) show reasonable agreement up to $Ro \simeq 2$, although differences in the functional forms of the relations—one being a cubic function, the other a log-linear function—lead to some subtle differences. These differences mean that stars in the peak shown in Figure 18 (which was made using the Noyes et al. 1984 relation) are re-distributed to slightly higher noise values when the relation of Mamajek & Hillenbrand (2008) is employed, giving the peak a long, gradually diminishing tail, and making it look less like the real histogram peak. For $Ro \gtrsim 2$ the relations diverge significantly, with Mamajek & Hillenbrand (2008) giving significantly lower values of R'_{HK} at a given Ro than Noyes et al. (1984). However, it is the differences at $Ro < 2$ that matter more for the observed distributions.

5. SIMULATED AND OBSERVED RESULTS AT *Kp = 14.5*

Figure 19 shows the distribution of stellar noise for the synthetic population stars in the range $Kp = 14.25$–14.75. There is a significant decrease in noise with increasing latitude, b,

which follows from clear trends in age, and hence the rotation periods, of the synthetic stars. From low to high latitude, the mean age increases monotonically from 4.5 to 5.5 Gyr, while the mean rotation period increases from 13 to 15 days. For intrinsic noise of 30–70 ppm 52% of the artificial stars lie at $b < 13°$, while at 17–21 ppm and 7–11 ppm the fraction drops to 47% and 42%, respectively. These clear trends are much more pronounced than those in the synthetic population results for $Kp = 11.5$–12.5, being much more similar to the observed trends as discussed in Section 3.5. This may be taken as another sign (Chaplin et al. 2011a) that the TRILEGAL-supplied distribution of fundamental stellar parameters for bright stars in the *Kepler* field differs in detail from actual values.

Comparison with the observed results for this $\times 10$ fainter sample than the $Kp = 11.5$–12.5 set considered earlier is best presented by a different approach. For the brighter sample, corresponding to the point design of the *Kepler* mission (Koch et al. 2010), the intrinsic stellar noise was the largest term, followed by the Poisson and other terms that in concert remained only slightly larger than the stellar noise. At the fainter sample the intrinsic stellar noise is similar, but the other terms grow such that the stellar noise is a minor contributor to the overall error budget. In this case the decomposition for intrinsic stellar noise would be much less stable. Since the decomposition even at 12th magnitude required finesse of multiple degeneracies, and resulted in small fractions of non-physical results (e.g., negative stellar variances), we opt here to only consider a forward consideration comparing observed and simulated results.

Figure 20 shows the relative distribution of the as-observed CDPP, contrasted to the distribution of simulated CDPP as pulled from Figure 16. The observed values and simulations are in reasonable agreement with a very similar mode, differing only in distribution details. Evaluated from values up to 300 ppm the observed and simulated CDPPs at $Kp = 14.5$ have medians of 80.7 and 78.9 ppm, respectively. With means evaluated for stars up to $3\times$ the median the results are 85.4 and 88.8 ppm for the observed and simulated stars, respectively.

6. PROSPECTS FOR CONFIRMATION

We have argued that much of the observed photometric variation in even the quiet *Kepler* stars arises from intrinsic variability through granulation and stellar activity on the timescales relevant here. Both the decomposition approach of Section 3, and the

simulation approach of Section 4 suggest a distribution function for stellar noise characterized by a broad (possibly bi-modal) peak at low intrinsic variability, and an extended tail to larger variations. Since we have contributed star-by-star measurements for the intrinsic variability it is possible to provide arguments for follow-up observations that could test these conclusions.

6.1. Derivation of Stellar Rotation Period from Kepler Data

Figure 9 suggested that qualitative differences may exist for the light curves coming from different portions of the intrinsic noise populations. In particular, light curves for stars selected based on noise from the extended tail as shown in Figure 8 should be amenable to derivation of stellar rotation periods from the *Kepler* light curves, e.g., from the approach of Mosser et al. (2009) applied for *CoRoT* data. The same set of stars could for consistency have $v\sin i$ measured with high-resolution spectroscopy. Confirmation that this set of stars is more rapidly rotating than the Sun would provide support for the primary assumption of this paper, that the noise for these stars is typically intrinsic, and that it arises from high activity associated with stellar youth and still rapid rotation.

6.2. Spectroscopic Measurement of Activity Indices

A primary component of the simulations of Section 4 involves model predictions of the R'_{HK} Ca H and K emission index. Measures for this could be obtained for the three ranges of intrinsic variability as in Figure 8 by observing, at high spectroscopic resolution, several stars from the 7–12, 14–19, and 30–50 ppm ranges. For these corresponding sets in Figure 18 the mean log R'_{HK} values are: -5.3, -5.2, and -4.9, respectively. Mean ages are, respectively, 6.6, 4.7, and 2.8 Gyr, while mean rotation periods are 13.9, 12.7, and 12.3 days. Our decompositions and simulations predict that stars drawn from these subsets will have progressively increasing levels of magnetic activity that serve as causal agents for the inferred photometric variability. The fraction of stars from Figure 18 as quiet as the Sun ($\leqslant 12.5$ ppm) is 23%, which is contrary to expectations (Basri et al. 2005) that two-thirds of solar-type stars would be as quiet as the Sun. The TRILEGAL simulations have only 24% of the solar-type stars older than 4.6 Gyr, and 52% are significantly younger than the Sun at <3 Gyr. The fraction of observed stars in Figure 8 below 12.5 ppm is also 23%. We note, however, that the simulations both at $Kp = 12$ and 14.5 have larger extended noise tails than the observations—consistent with the age distribution in the simulations being too young.

6.3. Asteroseismic Age Determinations

Perhaps the highest fidelity test to confirm the basic premises of this paper could be obtained by using *Kepler* short cadence data for a brighter subset of stars in these different intrinsic noise ranges to define stellar ages. Recent asteroseismic applications for the transiting exoplanet host HAT-P-7 (Christensen-Dalsgaard et al. 2010) with *Kepler* provided an age estimate of 2.14 ± 0.26 Gyr, while similar results using *HST* for HD 17156 (Gilliland et al. 2011) gave 3.2 ± 0.3 Gyr. Metcalfe et al. (2010) have provided a similarly accurate age estimate for KIC 11026764 near 6 Gyr good to 15%, with prospects in slightly evolved cases like this showing mixed modes for verifying the age even better. While it is unlikely that high fidelity age estimates will follow from the hundreds of dwarf stars currently having oscillation detections with *Kepler* (Chaplin et al. 2011a), it would be reasonable based on current results to expect such

results for about 100 targets. Obtaining these age determinations is a primary goal of the *Kepler* asteroseismology program, independent of the minor role having such would play in testing the premises in this paper.

7. SUMMARY

We have shown that the noise levels resulting for *Kepler* observations can be decomposed into a few terms: basics such as Poisson statistics and readout noise, an instrument term that depends on channel number over the 84 amplifiers, a temporal term that depends on specific observing conditions encountered during individual quarters of observation, and intrinsic stellar noise. The dominant term for roughly solar-type 12th magnitude stars in the overall noise budget is found to follow from the stars themselves. Excess instrument noise does exist, but is more-or-less in line with expectations, and contributes little to the overall noise within which *Kepler* planet searches must be conducted. By contrast the intrinsic stellar noise, although still very modest at less than 20 ppm for the highest concentration of stars, is a factor of two larger than had been budgeted for. This results in CDPP estimates for $Kp \sim 12$ that are 50% larger than anticipated.

We have shown via simulations of expected fundamental stellar parameters over the *Kepler* field of view, followed by projections of stellar rotation and resulting activity levels, that stellar variability consistent with that observed can be reproduced to first order. These simulations at $Kp \sim 12$ produce a broad distribution of stars with intrinsic noise levels over ~ 10–20 ppm that is consistent with that derived directly from the *Kepler* data.

CoRoT provided fundamental advances in time-series photometry securely establishing that most, if not all red giants are variable and reaching impressive new precision levels for 12th magnitude dwarfs (Aigrain et al. 2009) sufficient to allow searches for small planet transits. *Kepler* has taken this a large step further and is the first mission capable of quantifying the variability of large numbers of stars to the small levels by which the Sun is known to vary. *Kepler* will continue to provide exciting new insights into the astrophysics of quiet stars, and their galactic distributions. While we are not surprised to have learned new things from this new observational capability, the fact that the stars are more variable than expected has a significant influence on the ability to readily detect Earth-analog planet transits where the expected signal per transit is only a few times the inferred noise level on comparable timescales. Observing for a longer time baseline can compensate for the loss of transit detection sensitivity from the higher than anticipated stellar noise.

REFERENCES

Aigrain, S., Favata, F., & Gilmore, G. 2004, A&A, 414, 1139
Aigrain, S., Pont, F., Fressin, F., et al. 2009, A&A, 506, 425
Arnouts, S., Vandame, B., Benoist, C., et al. 2001, A&A, 379, 740
Basri, G., Borucki, W. J., & Koch, D. 2005, New Astron. Rev., 49, 478
Batalha, N. M., Borucki, W. J., Bryson, S. T., et al. 2011, ApJ, 729, 27
Batalha, N. M., Borucki, W. J., Koch, D. G., et al. 2010, ApJ, 713, L109
Beck, P. G., Bedding, T. R., Mosser, B., et al. 2011, Science, 332, 205
Bedding, T. R., Mosser, B., Huber, D., et al. 2011, Nature, 471, 608
Borucki, W. J., Koch, D. G., Basri, G., et al. 2011, ApJ, 736, 19
Brown, T. M., Latham, D. W., Everett, M. E., & Esquerdo, G. A. 2011, AJ, 142, 112
Bryson, S. T., Jenkins, J. M., Klaus, T. C., et al. 2010a, Proc. SPIE, 7740, 77401D
Bryson, S. T., Tenenbaum, P., Jenkins, J. M., et al. 2010b, ApJ, 713, L97
Caldwell, D. A., Kolodziejczak, J. J., Van Cleve, J. E., et al. 2010, ApJ, 713, L92
Cardini, D., & Cassatella, A. 2007, ApJ, 666, 393
Carter, J. A., Fabrycky, D. C., Ragozzine, D., et al. 2011, Science, 331, 562
Chaplin, W. J., Houdek, G., Appourchaux, T., et al. 2008, A&A, 485, 813
Chaplin, W. J., Kjeldsen, H., Bedding, T. R., et al. 2011b, ApJ, 732, 54
Chaplin, W. J., Kjeldsen, H., Christensen-Dalsgaard, J., et al. 2011a, Science, 332, 213
Christensen-Dalsgaard, J., Kjeldsen, H., Brown, T. M., et al. 2010, ApJ, 713, L164
Christiansen, J., & Machalek, P. 2010, Kepler Data Release 7 Notes, KSCI-19047-001 (Moffett Field, CA: NASA Ames Research Center)
Ciardi, D. R., von Braun, K., Bryden, G., et al. 2011, AJ, 141, 108
Cutri, R. M., Skrutskie, M. F., van Dyk, S., et al. 2003, The IRSA 2MASS All Sky Point Catalog, NASA/IPAC Infrared Science Archive, http://irsa.ipac.caltech.edu/applications/Gator/
Derekas, A., Kiss, L. L., Borkovits, T., et al. 2011, Science, 332, 216
Fröhlich, C., Andersen, B. N., & Appourchaux, T. 1997, Sol. Phys., 170, 1
Gilliland, R. L. 1985, ApJ, 299, 286
Gilliland, R. L. 2005, Instrument Science Report TEL 2005-02 (Baltimore, MD: STScI)
Gilliland, R. L. 2008, AJ, 136, 566
Gilliland, R. L., Jenkins, J. M., Borucki, W. J., et al. 2010, ApJ, 713, 160
Gilliland, R. L., McCullough, P. R., Nelan, E. P., et al. 2011, ApJ, 726, 2
Girardi, L., Bressan, A., Bertelli, G., & Chiosi, C. 2000, A&AS, 141, 371
Gould, A., & Eastman, J. 2011, arXiv:1102.1009v1
Haas, M. R., Batalha, N. M., Bryson, S. T., et al. 2010, ApJ, 713, 115
Hall, J. C., Henry, G. W., Lockwood, G. W., Skiff, B. A., & Saar, S. H. 2009, AJ, 138, 312

Harvey, J. 1985, in ESA Workshop, Future Missions in Solar, Heliospheric and Space Plasma Physics, ed. E. Rolfe & B. Battrick (The Netherlands: Noordwijk), 199
Holman, M. J., Fabrycky, D. C., Ragozzine, D., et al. 2010, Science, 330, 51
Huber, D., Stello, D., Bedding, T. R., et al. 2009, Commun. Asteroseismol., 160, 74
Ida, S., & Lin, D. N. C. 2004, ApJ, 604, 388
Jenkins, J. M. 2002, ApJ, 575, 493
Jenkins, J. M., Caldwell, D. A., Chandrasekaran, H., et al. 2010a, ApJ, 713, L87
Jenkins, J. M., Caldwell, D. A., Chandrasekaran, H., et al. 2010b, ApJ, 713, L120
Karoff, C. 2011, MNRAS, submitted
Kasting, J. F., Whitmire, D. P., & Reynolds, R. T. 1993, Icarus, 101, 108
Kjeldsen, H., & Bedding, T. R. 1995, A&A, 293, 87
Kjeldsen, H., & Bedding, T. R. 2011, A&A, 529, 8
Knaack, R., Fligge, M., Solanki, S. K., & Unruh, Y. C. 2001, A&A, 376, 1080
Koch, D. G., Borucki, W. J., Basri, G., et al. 2010, ApJ, 713, L79
Kolodziejczak, J. J., Caldwell, D. A., Van Cleve, J. E., et al. 2010, Proc. SPIE, 7742, 77241G
Kurtz, D. W., Cunha, M. S., Saio, H., et al. 2011, MNRAS, 414, 2550
Lissauer, J. L., Fabrycky, D. C., Ford, E. B., et al. 2011, Nature, 470, 53
Lockwood, G. W., Skiff, B. A., Henry, G. W., et al. 2007, ApJS, 171, 260
Mamajek, E. E., & Hillenbrand, L. A. 2008, ApJ, 687, 1264
Metcalfe, T. S., Basu, S., Henry, T. J., et al. 2010, ApJ, 723, 213
Mosser, B., Baudin, F., Lanza, A. F., et al. 2009, A&A, 506, 245
Noyes, R. W., Hartmann, L. W., Baliunas, S. L., Duncan, D. K., & Vaughan, A. H. 1984, ApJ, 279, 763
Osmer, P. S., Kennefick, J. D., Hall, P. B., & Green, R. F. 1998, ApJS, 119, 189
Perryman, M. A. C., Lindegren, L., Kovalevsky, J., et al. 1997, A&A, 323, L49
Press, W. H., Teukolsky, S. A., Vetterling, W. T., & Flannery, B. P. 1992, Numerical Recipes in Fortran (2nd ed.; Cambridge: Cambridge Univ. Press)
Radick, R. R., Lockwood, G. W., Skiff, B. A., & Baliunas, S. L. 1998, ApJS, 118, 239
Radick, R. R., Lockwood, G. W., Skiff, B. A., & Thompson, D. T. 1995, ApJ, 452, 332
Radick, R. R., Thompson, D. T., Lockwood, G. W., Duncan, D. K., & Baggett, W. E. 1987, ApJ, 321, 459
Robin, A. C., Reylé, C., Derrière, S., & Picaud, S. 2003, A&A, 409, 523
Schlegel, D. J., Finkbeiner, D. P., & Davis, M. 1998, ApJ, 500, 525
Skumanich, A. 1972, ApJ, 171, 565
Schwarzschild, M. 1975, ApJ, 195, 137
van Cleve, J. E., & Caldwell, D. A. 2009, Kepler Instrument Handbook, KSCI-19033-001 (Moffett Field, CA: NASA Ames Research Center)
Welsh, W. F., Orosz, J. A., Aerts, C., et al. 2011, ApJS, 197, 4